

# Validation of Fault Displacements from Dynamic Rupture Simulations against the Observations from the 1992 Landers Earthquake

Yongfei Wang<sup>\*1</sup>  and Christine Goulet<sup>1</sup> 

## ABSTRACT

Coseismic fault displacements in large earthquakes have caused significant damage to structures and lifelines on and near fault lines. Coseismic displacements represent a real threat, especially to distributed infrastructure systems. For infrastructure systems that can not avoid active faults, engineering displacement demands are defined using probabilistic fault-displacement hazard analyses (PFDHA). However, PFDHA models are sparse and poorly constrained partly due to the scarcity of detailed fault-displacement observations. Advancements in dynamic rupture simulation methods make them an attractive approach to address this important issue. Because fault displacements can be simulated for various geologic conditions as constrained by current knowledge about earthquake processes, they can be used to supplement the observation datasets. In addition to providing on-fault displacements, when used with appropriate constitutive models for the bulk medium, they can capture off-fault distributed inelastic deformations as well. For viable extrapolation, simulations must first be validated against data. In this article, we summarize the calibration and validation of the dynamic rupture model against the observations of the well-documented 1992 Landers earthquake. We defined a preferred model that reproduces several first-order fault-displacement metrics such as the on-fault partition of the total displacement, the mean fault-zone width, and the location of the peak displacement. Simulated ground motions consistent with the observations ensure that all physics important to modeling have been properly parameterized. For the extrapolation, we generated a suite of dynamic rupture models to quantify expected fault-displacement metrics, their intercorrelations, and magnitude dependencies, which are in part supported by the Landers and other recent earthquakes. Our validation and extrapolation exercise paves the way for using dynamic rupture modeling to quantitatively address fault-displacement hazard on a broader scale. The results are promising and are expected to be useful to inform PFDHA model development.

## KEY POINTS

- We propose a process for predicting fault displacements using dynamic rupture modeling.
- We compare a dynamic rupture model against observations from the Landers earthquake.
- The results show promise for using dynamic rupture models of fault displacements in probabilistic assessments.

## Supplemental Material

## INTRODUCTION

Coseismic fault displacements in large earthquakes have caused significant damage to structures and lifelines located on or near fault lines. Examples include severely damaged bridges, dams, and tunnels in the 1999 Chi-Chi earthquake, pancaked buildings

in the 1999 Kocaeli earthquake, distorted railroads in the 1975 Guatemala earthquake, and ruptured water lines during the 2019 Ridgecrest earthquake sequence. Fault displacements therefore represent a real threat, especially to distributed infrastructure systems that can be intersected by faults in more than one location. This seismic hazard has been addressed by recommendations and regulations restricting construction near active fault zones. An example is the Alquist-Priolo Earthquake Fault

1. Southern California Earthquake Center, University of Southern California, Los Angeles, California, U.S.A.,  <https://orcid.org/0000-0003-1121-7726> (YW);  <https://orcid.org/0000-0002-7643-357X> (CG)

\*Corresponding author: [yongfeiw@usc.edu](mailto:yongfeiw@usc.edu)

**Cite this article as:** Wang, Y., and C. Goulet (2021). Validation of Fault Displacements from Dynamic Rupture Simulations against the Observations from the 1992 Landers Earthquake, *Bull. Seismol. Soc. Am.* **XX**, 1–21, doi: [10.1785/0120210082](https://doi.org/10.1785/0120210082)

© Seismological Society of America

Zoning Act (AP Act, appendix A of [California Geological Survey \[CGS\], 2018](#)) in the state of California—a law enacted following the 1971 San Fernando earthquake. The AP Act requires, for example, that a new construction used for human occupancy be more than 15 m (50 feet) away from a mapped fault trace or, if within that zone, it requires that a comprehensive site-specific investigation be performed. Similar legislations have been implemented in Japan, New Zealand, and China as well. However, there are situations for which the avoidance of the fault zone is not possible or not practical (e.g., gas and water supply and distribution networks, roads, certain dams). Thus, guidance on the potential fault-displacement hazard is needed to inform engineering design.

For ground-motion hazard, the design is informed by a combination of deterministic and probabilistic seismic hazard analyses (DSHA and PSHA). PSHA is well established for ground-motion hazard, but its counterpart for probabilistic fault-displacement hazard analysis (PFDHA) is not as mature. The PFDHA approach gained broader interest during the assessment of the Yucca Mountain nuclear waste repository site ([Stepp et al., 2001](#); [Youngs et al., 2003](#)). It has since been extended to include more fault-displacement data from various fault mechanisms and to include improved uncertainty quantification approaches ([Moss and Ross, 2011](#); [Petersen et al., 2011](#); [Chen and Petersen, 2019](#); [Nurminen et al., 2020](#)). However, compared with the well-developed empirical ground-motion models (GMMs, also known as GMPEs), empirical fault-displacement models are sparse and poorly constrained, partly due to the paucity of detailed high-resolution fault-displacement observations, despite recent large database building efforts (e.g., [Sarmiento et al., 2019](#); [Baize et al., 2020](#)). The reasons for this paucity of data include (1) a low occurrence of earthquake ruptures that reach the surface (tend to be from a subset of large-magnitude events, and large-magnitude events are rare), (2) a long recurrence period between earthquakes with a collocated surface rupture (~ hundreds of years) that does not allow the comparison of potentially similar events, and (3) a technical difficulty of exhaustively collecting perishable fault displacements over very large areas. These data limitations make the use of earthquake rupture simulations an attractive solution to support PFDHA modeling as part of the Fault Displacement Hazard Initiative (FDHI; [Bozorgnia et al., 2021](#)).

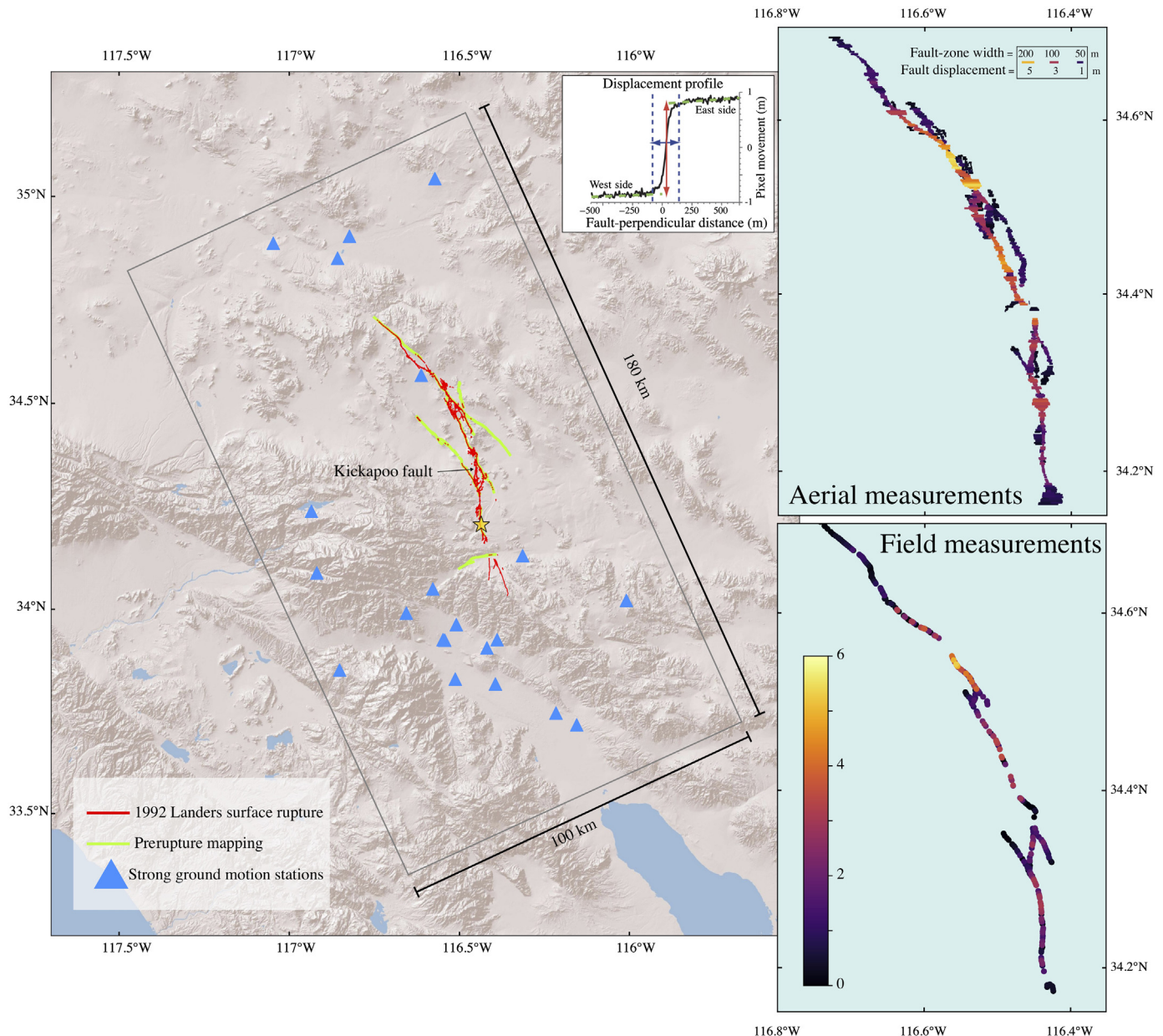
Before simulation models can be used, they must first be validated against observations for which detailed datasets exist. The validated models can then be used to generate scenarios and simulated datasets for events we have not yet observed. A similar approach was used to support the development of GMMs. For example, [Day et al. \(2008\)](#) simulated the effect of sedimentary basin on long-period response spectra, [Donahue and Abrahamson \(2014\)](#) developed a hanging-wall effect model based on simulations performed with the Southern California Earthquake Center (SCEC) Broadband

Platform (BBP, [Maechling et al., 2015](#)), and [C. A. Goulet et al. \(2021\)](#) used BBP simulations to model the magnitude scaling for the central and eastern United States ([Dreger et al., 2015](#); [Goulet et al., 2015](#)). Results from these simulations contributed to the NGA-East GMMs.

In this study, the physics-based model used is referred to as the dynamic rupture model; it constructs spontaneously evolving earthquake ruptures under mechanical causative conditions (e.g., fault geometry, friction law, stress condition, and surrounding rock properties). It makes it ideal for the simulation of displacements, which vary along the fault plane due to the dynamic response to imposed stresses. Our project (i.e., FDHI) involves the application of the dynamic rupture model to California events, its validation against well-documented case histories, and its use to predict displacements for scenarios and events we have not yet experienced. Those synthetic displacement datasets can, in turn, be used alone or combined with empirical observations to support PFDHA model developments.

In this article, we present the validation and calibration of our method against the 1992 M 7.3 Landers earthquake. We selected this event for the first validation exercise due to the high quality and relative completeness of its displacement and ground-motion data. The Landers earthquake is the third-largest California event of the twentieth century. It occurred within a roughly 70 km long zone of north-northwest-trending dextral faults accommodated by the eastern California shear zone (Fig. 1). The Landers earthquake was initiated near the southern end and propagated unilaterally toward the northern end. Field mapping by geologists revealed particularly complex patterns of surface rupture (Fig. 1; [Liu et al., 2003](#)). Comparison of the surface rupture with previously mapped fault traces (prerupture mapping, Fig. 1) shows that the Landers event spanned two (previously) disconnected groups of faults with the previously unknown Kickapoo fault (indicated by an arrow in Fig. 1). This comparison of pre- and post-event surface expression highlights the complexity and the difficulty in predicting future displacements from prerupture fault mapping (in this case, as defined in the AP maps at the time). It also highlights the motivation behind our choice of geometry for the validation, which is a simplified model, similar to what is documented in the AP maps. In that sense, the validation is performed not only with the end goal in mind of not reproducing every single displacement observed in Landers but also to capture the general displacement characteristics observed, using an ensemble of simulation results. This is consistent with how PFDHA will be used, that is, based on a scenario defined by a magnitude and a rough definition of the fault location and geometry. This is also consistent with how GMMs are developed and used, based on scenario parameters.

In addition to the detailed field geological mappings (e.g., [Liu et al., 2003](#)), a high-resolution fault-displacement profile was provided through the Co-registration of Optically Sensed



Images and Correlation (COSI-Corr) technique, which performs aerial measurements of surface deformation over a wider aperture than that of the field mapping (Milliner et al., 2015, 2016). Such a technique overcomes the limitation that traditional field mapping is unable to capture the complete fault displacements at high resolution along the entire fault rupture region, including right along the fault strand and at distances away from it (referred to as “off-fault deformation” [OFD]). In this study, the term OFD is used interchangeably with the term off-fault displacement that is often used in PFDHA (e.g., Petersen et al., 2011; Nurminen et al., 2020) to account for distributed off-fault small-scale fractures. The distributed OFDs, while practically challenging to collect, can be important to engineering applications sensitive to strains such as high-speed rail (e.g., Yoon et al., 2020). Figure 1 illustrates the difference between aerial and field observations maps for Landers.

**Figure 1.** Map of the 1992 Landers earthquake source region. Red lines in the left geographic map indicate the surface rupture strands involved in Landers, and green ones indicate the pre-rupture mapping in this region. Both datasets are compiled into the Fault Displacement Hazard Initiative (FDHI) Database (Sarmiento et al., 2019). The black arrow points out the location of the Kickapoo fault. Blue triangles are seismic stations at which ground motions were recorded. The upper small panel shows an example of fault displacements interpreted from aerial measurements (Milliner et al., 2015). The two right panels illustrate the fault displacements from (top) aerial and (bottom) field measurement (Sarmiento et al., 2019). The fault-zone width (FZW) is also shown by the length of the horizontal bar in the right upper panel.

The aerial measurements capture the presence of OFD, and this aperture coverage leads to larger total displacement than those strictly observed on the fault by field measurements (Milliner et al., 2015, 2016). The distributed OFD in the forms of warping,

granular flow, rigid-block rotation, secondary faulting, and microfracturing is common in single coseismic events and over repeated earthquake cycles (e.g., [Rockwell et al., 2002](#); [Oskin et al., 2007](#); [Zinke et al., 2014](#); [Teran et al., 2015](#)). The COSI-Corr technique is also capable of providing strain localization information through the interpretation and definition of a fault-zone width (FZW) across which the fault displacement shows a gradual transition from large near the fault trace to negligible at a distance from it (Fig. 1). The existence of OFD has a significant implication for fault-displacement model development, and the incorporation of the complete near-field deformation pattern will lead to a more reliable fault-displacement hazard prediction. The advent of aerial datasets and COSI-Corr are now enabling the integration of such strain fields into PFDHA models.

In this study, we develop a dynamic rupture model for Landers and validate the fault displacements against the available empirical datasets. Although our focus is on displacement, we also perform a validation of the ground motions resulting from that model to confirm that the physics has been appropriately modeled and parameterized. The validation step involves sensitivity analyses and a calibration of the model parameters to be used to capture at least some of the modeling uncertainties. With the intent of later generating simulations for California events not yet observed, we develop a suite of dynamic rupture models (varied magnitudes) by relaxing the fault small-scale geometry and stress condition, introducing a certain level of extrapolation of the Landers-based models. The dynamic rupture model was recently successfully applied to reproduce the observed fault-displacement profile of the 2010 M 7.0 Darfield earthquake ([Dalguer et al., 2019](#)) —a notably complex fault. In contrast, our simulations are designed to be general in their parameterization and not detailed to the point that the results apply to a single specific fault modeled in detail, so as to supplement the empirical datasets and provide guidance for PFDHA modeling. In addition, this type of simulation is computationally demanding, and simplifications in modeling are necessary (as described later) to make the scope of work tractable, provided that several suites of large-scale simulations are to be performed.

## DYNAMIC RUPTURE MODEL SETUP FOR THE LANDERS SCENARIO

### Simulations in support of PFDHA modeling

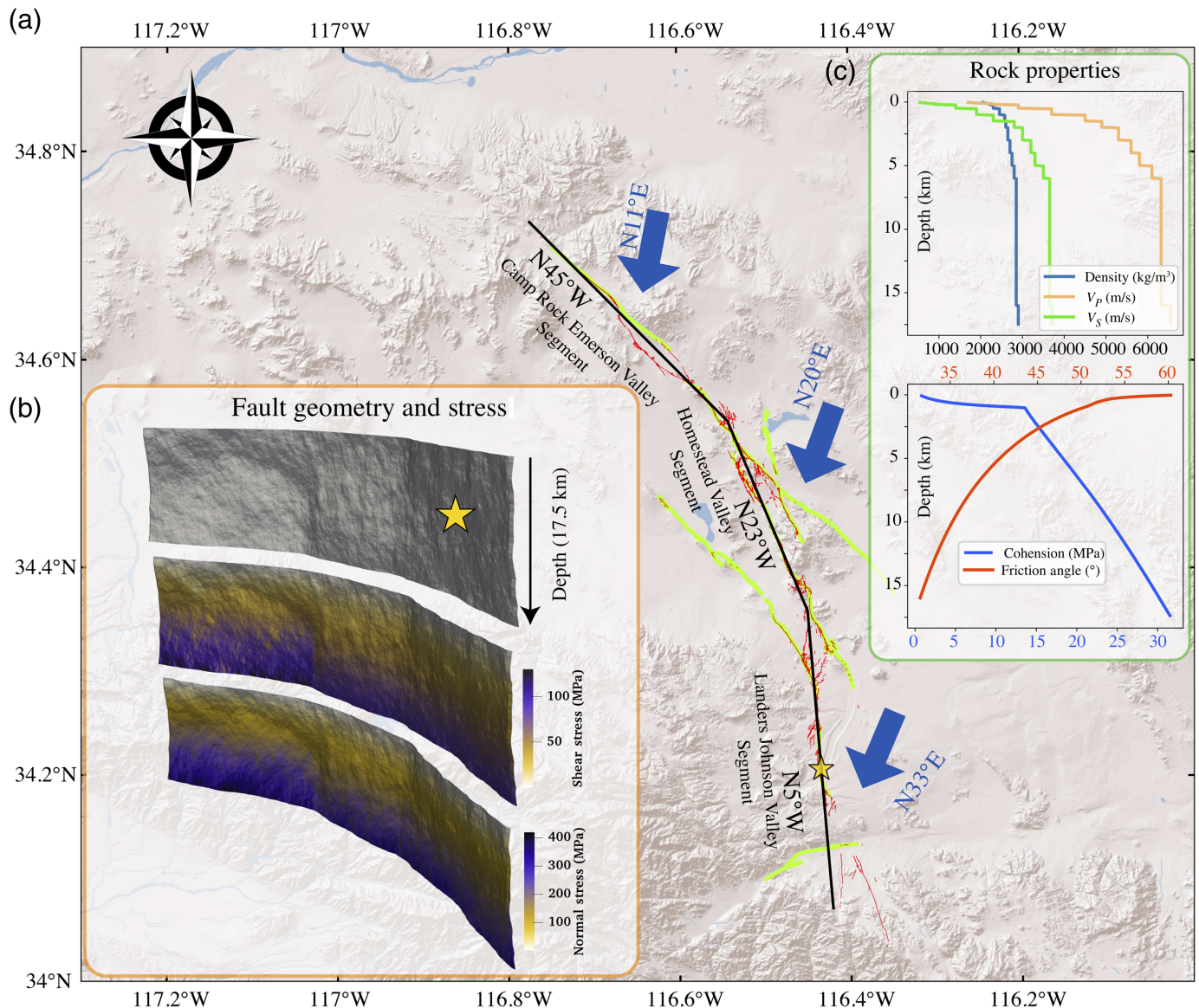
The motivation for our project is to support PFDHA modeling by supplementing the limited empirical displacement dataset with simulation data. The forward simulations will need to cover, for example, different fault geometries, magnitudes, and states of stress that are representative of expected future events in California, our focus region. To be useful in informing PFDHA modeling scaling, the simulations must be specific enough to capture realistic fault ruptures while being general enough to capture the key features of the displacement field,

without being fault specific. Our modeling strategy is to develop a suite of models and simulations that together will capture the expected displacement of future events. Before the simulations are used by PFDHA modelers, the underlying models must be validated against empirical observations. By performing the validation in a manner consistent with how the forward simulations will be generated (general ensemble models), we ensure a consistency between the validated models and the forward simulations. That is, the goal is to make sure that a calibrated ensemble of simulations can capture the trends in observations (as opposed to capturing every displacement detail from the single realization Landers event). This type of validation strategy was successfully used for ground-motion validation of the SCEC BBP ([Dreger et al., 2015](#); [Goulet et al., 2015](#)). In the forward sense, the PFDHA models will require simple input parameters such as  $M$ , fault dimensions and dip, and fault mechanism; so our goal is to generate suites of events that span these attributes.

The faults that ruptured during the Landers earthquake are very complex; they consist of curved, branched, and segmented nonplanar faults (Fig. 1). Although fairly complex fault systems have been modeled by dynamic rupture ([Aochi et al., 2003](#); [Tago et al., 2012](#); [Dalguer et al., 2019](#); [Wollherr et al., 2019](#)), such that they capture the complexity of the real event, they remain event-specific. Our application requires modeling simplifications to meet the goals described earlier and also to be computationally tractable. In the remainder of the current section, we describe our modeling choices to meet those goals by focusing on the dynamic rupture for simulating the 1992 Landers earthquake. To build a spontaneously evolving dynamic rupture model, a number of causative physical modeling choices and assumptions are required that can be summarized in the following general categories of so-called “ingredients” ([Harris et al., 2009](#)): (1) fault geometry and initial stress condition, (2) fault failure criterion (fault constitutive law that specifies the condition under which the fault is allowed to slip), and (3) surrounding material (rock) properties. To develop dynamic rupture models that are readily extendable to other scenarios and events, the models are based on relatively simple physics models and parameterized following general criteria informed by past Landers simulation studies, as described later. The choice of modeling assumptions and parameter values were selected following suites of sensitivity analyses. We defined a preferred model, selected to be most representative of the as-observed Landers event, and developed a suite of ensemble models representing plausible earthquakes of varying magnitude along the same base problem.

### Fault geometry and initial stress condition

Consistent with our simulation philosophy, we first define a simplified geometry for the Landers event, using the rough prerupture mapped fault traces as a guide. The three-segmented connected fault was originally developed by [Wald and Heaton](#)



(1994) and followed by several seismologists (e.g., Cohee and Beroza, 1994; Olsen *et al.*, 1997). Our simplified model (Fig. 2a) consists of three linear segments loosely fitting the following faults: the Landers Johnson Valley Segment (LJVS) in the south where the rupture nucleated, the Homestead Valley Segment (HVS) in the central part of the fault, and the Camp Rock Emerson Valley Segment (CREVS) in the north (black line in Fig. 2a). Their strike azimuths are N5°W, N23°W, and N45°W from the south to the north, respectively, leading to a fault length of 84 km with two kinks roughly at third-lengths. The strike-slip fault is modeled from the surface to a depth of 17.5 km (Fig. 2b).

To make our fault plane more realistic, we superimposed a geometrically self-similar roughness on the original planar geometry (Fig. 2b). This effectively improves the along-strike variability to be more consistent with observed data, as recommended by Bruhat *et al.* (2020). The fault roughness level is defined by the amplitude-to-wavelength ratio  $\alpha$

**Figure 2.** Simulation model setup. (a) Landers surface rupture strands (thin red lines), prerupture mapping (green lines), and the simplified three-segment fault line defined for the simulation (thick black line). Blue arrows indicate the orientations of the horizontal maximum principal stresses on different segments. (b) The lower left panel shows the fault-plane model, which includes small-scale fault roughness, with shear and normal stress projected on the resulting complex fault surface. (c) The upper right panel shows the rock properties, including depth variable density, P- and S-wave velocities, cohesion, and friction angle, which are used for the dynamic rupture simulation. The color version of this figure is available only in the electronic edition.

(equation A1 in Shi and Day, 2013) for which a value between  $10^{-3}$  and  $10^{-2}$  is proposed to correlate with the fault maturity (Power and Tullis, 1991; Sagy and Brodsky, 2009), as wear processes from repeated slip decrease  $\alpha$  in mature faults. Fault maturity can be inferred from fault structural complexities, coseismic rupture speed, and the ratio of deep slip to

surface slip (Dolan and Haravitch, 2014; Perrin *et al.*, 2016). It is noted that a quantitative relationship between fault roughness level and fault maturity has not been established to date due to lack of data and relies on a qualitative assessment. Based on documentation of the subshear rupture velocity, shallow slip deficit (SSD), and appreciable structural complexity from the 1992 Landers earthquake (Sieh *et al.*, 1993; Wald and Heaton, 1994; Fialko, 2004; Dolan and Haravitch, 2014), we set  $\alpha = 0.05$  to represent a fault with a relatively low maturity. In contrast, a more structurally mature fault such as the single prominent fracture surface of the Punchbowl fault was attributed a value of  $\alpha = 0.001$  based on laboratory tests from field samples (Chester *et al.*, 2004).

To construct the initial stress condition, we essentially follow Wollherr *et al.* (2019) and adapt their stress computation to our own geometry. The vertical principal stress is defined as an intermediate principal stress  $\sigma_2$  that is an average of the horizontal maximum and minimum principal stresses (i.e.,  $\sigma_2 = (\sigma_1 + \sigma_3)/2$ ). It varies linearly with depth as the difference between lithostatic pressure and hydrostatic pore-fluid pressure:

$$\sigma_2(h) = \int_0^h \rho(z)gdz - \rho_wgh \quad (1)$$

with gravity  $g = 9.81 \text{ m/s}^2$ , depth-dependent rock density  $\rho(z)$ , water density  $\rho_w$ , and depth  $h$ . The difference between  $\sigma_1$  and  $\sigma_2$  ( $\Delta\sigma = \sigma_1 - \sigma_2$ ) corresponds to the radius of the horizontal Mohr–Coulomb stress circle, which implies:

$$\tau^s = \sin(2\theta)\tau^n = \sigma_2 - \cos(2\theta), \quad (2)$$

in which  $\theta$  is the angle of the horizontal maximum principal stress with the fault plane, and  $\tau^s$  and  $\tau^n$  are shear and normal stresses projected on the fault plane. A relative prestress ratio  $R$  is defined as the fault stress drop over the fault strength drop:

$$R = \frac{\tau^s - \mu_d\tau^n}{\mu_s\tau^n - \mu_d\tau^n}, \quad (3)$$

in which  $\mu_s$  and  $\mu_d$  are static and dynamic friction coefficient from the slip-weakening friction law we adopted in this study (in the Fault Failure Criterion section). By combining equations (2) and (3),  $\Delta\sigma$  is obtained as a function of  $R$ , and  $\sigma_1$  and  $\sigma_3$  are accordingly derived.  $R$  can be chosen through numerical experiments with the observational constraints of seismic moment and rupture velocity. Furthermore, it is noted that the ratio between the initial shear and normal stresses are exclusively determined by  $R$ ; they are independent of the stress and fault-plane orientations. For simplicity, we maintain a constant  $R = 0.4$  along the full length of the fault as our preferred model. The orientations of the two horizontal principal stresses are taken directly from Wollherr *et al.* (2019), with the maximum principal stresses imposed at N11°E, N20°E, and

N33°E orientations for CREVS, HVS, and LJVS, respectively (Fig. 2a). This makes the northern CREVS the least favorable segment (56° between the fault and the maximum principal stress) characterized by a combination of larger shear and normal stresses relative to the other two segments at any given depth (Fig. 2a). This model setup implies a larger potential stress drop on CREVS (for frictional coefficients set equal for all faults), which is consistent with the observation of a substantial amount of slip occurring near the CREVS and HVS connection (Liu *et al.*, 2003; Milliner *et al.*, 2015), something also revealed in inversion studies (e.g., Cohee and Beroza, 1994; Wald and Heaton, 1994; Olsen *et al.*, 1997).

The dynamic rupture is nucleated on the LJVS using a circular zone with a 3 km radius at a depth of 7 km (yellow star in Fig. 2). Within this zone, the rupture is forced radially outward with a fixed slow rupture velocity of 2 km/s. Beyond that nucleation region, the rupture is allowed to spontaneously propagate.

### Fault failure criterion

In this study, we use a linear slip-weakening friction law (e.g., Ida, 1972) in which the shear stress  $\tau^s$  is bounded by the fault strength  $\tau^c$  defined as

$$\tau^s \leq \tau^c = \begin{cases} c_0 + \mu_s - (\mu_s - \mu_d)l/D_c\tau^n, & l \leq D_c \\ c_0 + \mu_d\tau^n, & l > D_c \end{cases}, \quad (4)$$

in which  $\mu_s$  and  $\mu_d$  are static and dynamic friction coefficients, respectively, and  $D_c$  is the critical slip-weakening distance,  $l$  is the slip, and  $c_0$  is the frictional cohesion. All the frictional parameters are set constant across the fault plane with values listed in Table 1. We set the static friction coefficient  $\mu_s = 0.5$  on LJVS and HSV and to 0.6 on CREVS, consistent with the regionally inferred effective value of 0.6 by Gross and Kisslinger (1997). The slightly increased value on CREVS is imposed so that the fault strength is over the peak shear stress, which prevents the rupture from nucleating on this specific segment. The dynamic friction coefficient  $\mu_d$  is set to 0.2 across the fault, and the critical slip-weakening distance  $D_c$  is 0.6 m, close to that used in previous studies (Olsen *et al.*, 1997; Wollherr *et al.*, 2019). These parameters are defined in a zone of 84 km long and 14 km deep, beyond which the friction linearly increases to infinity (i.e., to form an unbreakable boundary). These parameters along with the  $R$  ratio (0.4) synergically facilitate a sustained rupture with an observationally consistent seismic moment of  $6\text{--}16 \times 10^{19} \text{ N}\cdot\text{m}$  and rupture velocity of 2.5–2.9 km/s (Cohee and Beroza, 1994; Wald and Heaton, 1994; Cotton and Campillo, 1995).

The material in the shallow crust transitions from ductile in the uppermost crust (top few km) to brittle in the remaining seismogenic zone. The main purpose of the shallow ductile layer is to increase energy dissipation. This makes the friction properties have a depth dependence (e.g., Brune and Anooshehpour, 1998; Day and Ely, 2002). In the rate-and-state

TABLE 1  
**Summary of Modeling Parameters**

Model Parameter	Landers Johnson Valley Segment	Homestead Valley Segment	Camp Rock Emerson Valley Segment
Fault orientation (°)	N5°W	N23°W	N45°W
Maximum principal stress orientation (°)	N33°E	N20°E	N11°E
Static friction coefficient	0.5	0.5	0.5
Dynamic friction coefficient	0.2	0.2	0.2
Critical slip distance (m)	0.6	0.6	0.6
$R$ (Preferred model)	0.4	0.4	0.4
$R$ (Ensemble models)	0.45 0.5 0.35	0.45 0.5 0.35	0.35 0.4 0.25

The preferred model involves a single set of parameters, and the ensemble models consist of 48 individual models spanning four sets of  $R$  ratios and 12 realizations of the fault roughness.

friction framework, this layer has been proposed to follow a velocity-strengthening mechanism (Kaneko *et al.*, 2008) that is supported by laboratory experiments (Marone, 1998), and field observations of interseismic creep (Lindsey *et al.*, 2014) and shallow afterslip following large earthquakes (Perfettini and Avouac, 2007). We set the frictional cohesion  $c_0$  (in the slip-weakening law) to linearly decay from 1 MPa at the surface to zero below 3 km to mimic the ductile-to-brittle transition. These modeling choices are consistent with our goal to keep the model as simple as possible while making sure it produces an appropriate description of aggregate displacement at the surface. The near-surface friction property along with the near-surface stress condition and inelasticity model influence the fault displacement in a coupled mode; the effect of a high friction parameter can be traded off by a large stress or a weakly inelastic material. Because the fault friction is poorly constrained, its value is based on the aforementioned stress conditions and selected so as to make displacement values consistent with the observations.

## Rock properties

During an earthquake, some of the energy dissipation comes from inelastic deformations. The deformations are expected to be larger in the near-fault area where the stress concentration and release are the largest. Geodetic-based studies have inferred that the slip at depth is systematically larger than at the surface—a phenomenon described earlier as SSD. That SSD, as well as the OFD, is attributed to the shallow distributed inelastic deformation (e.g., Kaneko and Fialko, 2011; Roten *et al.*, 2017). Both SSD and OFD, sensitive to the material strength beyond which rock inelastically deforms, were observed in the Landers earthquake. Theoretically, lower material strengths lead to larger SSD and OFD (Roten *et al.*, 2017). We model the SSD and OFD using a plasticity model borrowed from continuum mechanics. Specifically, we follow Roten *et al.* (2017) and implement the generalized Hoek–Brown model (Hoek *et al.*, 2002) that accounts for preexisting cracks in rock volumes by introducing the Geological Strength Index (GSI). Detailed descriptions of the

Hoek–Brown model can be found in Hoek *et al.* (2002). For our purpose of simplicity, we do not implement a low-velocity fault zone as Roten *et al.* (2017) did. We tuned the properties to match displacement observations, selecting an average quality rockmass (defined in Roten *et al.*, 2017) with GSI = 50 (on the surface), intact material constant  $m_i = 12$ , and unconfined compressive strength  $\sigma_{ci} = 80$  MPa, corresponding to disintegrated but weakly interlocked limestone. GSI is set to linearly increase from its value of 50 at the surface to 100 (intact rock) at 1 km and deeper, implying that the rockmass behavior approaches that of intact rock at those depths (Marinos *et al.*, 2005). Thus, the inelastic effect is concentrated in the top 1 km. We implement depth-variable equivalent friction and inelastic cohesion (lower panel of Fig. 2c), which approximate the Hoek–Brown yield surface with a commonly used Drucker–Prager criterion (Drucker and Prager, 1952) through the relations in Hoek *et al.* (2002). It is noted that the sharp transition in cohesion in Figure 2c is caused by the saturation of GSI at 1 km. The plasticity model is a simplification of the more complex physics at play (involving brittle failures), but it is computationally efficient and sufficient for our specific application. The surrounding volume is defined by a 1D-layered elastic velocity model, as illustrated in the upper panel of Figure 2c. The velocity model was adopted from the SCEC BBP as a representative of the structure of the Mojave Desert (Goulet *et al.*, 2015).

## Numerical approach and performance

We simulate fault displacements by numerically solving the 3D elastoplastic spontaneous rupture propagation problem with the Support Operator Rupture Dynamics (SORD) code (Ely *et al.*, 2009; Shi and Day, 2013; Wang and Day, 2020). This generalized finite-difference method has been used in numerous studies of spontaneous dynamic ruptures and ground motions (e.g., Wang and Day, 2017; Vyas *et al.*, 2018; Wang *et al.*, 2019; Savran and Olsen, 2020). SORD has also been verified through a number of benchmarks, including testing with small-scale fault geometrical roughness, plasticity, and thermal pressurization as part of the SCEC-based technical

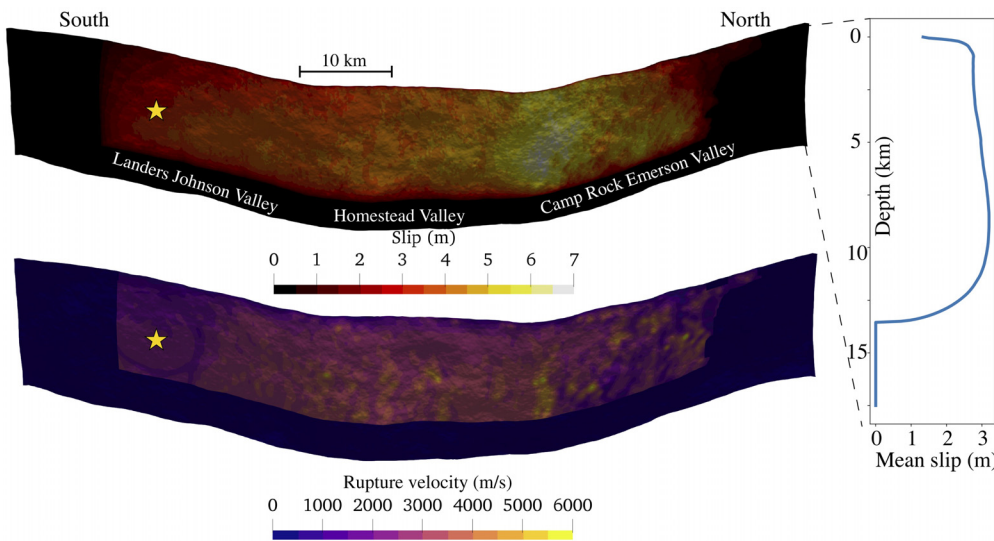


**Figure 3.** (Left top) Coseismic slip and (left bottom) rupture velocity for the preferred model, with the location of the hypocenter indicated by a yellow star. The right plot shows the mean slip averaged over the strike as a function of depth. The color version of this figure is available only in the electronic edition.

activity group on dynamic code rupture verification (Harris *et al.*, 2009; Harris *et al.*, 2018). The cohesive zone requires at least  $\sim 5$  grid points for ensuring numerical convergence (Day *et al.*, 2005) and is well resolved by our discretization (Fig. S1, available in the supplemental material to this article). Considering the minimum shear-wave velocity of 550 m/s, we estimate that our numerical solution provides accurate waveforms for frequencies up to roughly 1 Hz. The model contains 1.9 billion hexahedral elements and simulates a 60 s rupture. The computation takes  $\sim 3$  hr using 8192 processors on Frontera at the Texas Advanced Computing Center and on Theta at the Argonne Leadership Computing Facility. Both the systems were used in this project.

## RESULTS

### Preferred dynamic model

In this section, we further describe our preferred model intended to best represent the Landers event (given the modeling assumptions and choices described earlier). The seismic moment ( $10.7 \times 10^{19}$  N · m corresponding to M 7.3) is within the range of observational studies ( $6 \times 10^{19}$ – $16 \times 10^{19}$  N · m); the slip-weighted stress drop is 14.0 MPa, also in agreement with that used in previous dynamic modeling studies (e.g., Peyrat *et al.*, 2001; Wollherr *et al.*, 2019) and kinematic source modeling studies (Bouchon *et al.*, 1998; Day *et al.*, 1998). Figure 3 illustrates the coseismic slip and rupture velocity over the whole irregular fault plane. The peak slip exceeds 6 m near the smoothed kink between HVS and CREVS (around 40 km away from the hypocenter). This simulated result is supported by the observations (Perrin *et al.*, 2016) that the zone of the largest fault displacement and the hypocenter location are

uncorrelated; they can be close to each other (e.g., 1999 Hector Mine and 2010 El Mayor-Cucapah) but more often distant (e.g., 1992 Landers and 2002 Denali). The simulated depth-varying mean slip in Figure 3 shows that the slip is substantially tapered at the top 1 km, and that a strong plastic effect occurs at this depth, leading to an SSD of  $\sim 40\%$ , within the range (30%–60%) estimated for the Landers earthquake (Kaneko and Fialko, 2011). In addition to those observation-consistent static deformation parameters, the rupture velocity is nearly 3 km/s at the seismogenic depth and as slow as 1–2 km/s at the shallow depth

(Fig. 3), which is also in agreement with previous finite-fault study findings (Cohee and Beroza, 1994; Wald and Heaton, 1994; Cotton and Campillo, 1995). In all, results for both the simulated static and kinematic parameters are consistent with those estimated in previous Landers studies, suggesting that our preferred dynamic model captures the first-order characteristics of the Landers earthquake in the aspects of overall deformation and seismic radiation.

The simulated horizontal surface deformation near the fault trace (Fig. 4) shows an overall dextral shear movement (for clarity, we show the north-south and east-west components next to each other.). The sinuosity on the fault trace (Fig. 4) illustrates the effect of the self-similar fault roughness applied to the three-segment model. For the purpose of this project, we define two sets of fault displacements: on-fault displacement that is measured on the fault trace analogous to the field estimates and total displacement that is measured over a wider aperture analogous to the aerial estimates. To mimic the subpixel correlation process used in Milliner *et al.* (2015), we devised a sliding window (gray box in Fig. 4) with a 2 km fault-perpendicular width and a 200 m fault-parallel length. Inside the window, simulated fault-parallel displacements (computed from the horizontal deformation and the averaged strike orientation of the local fault trace) are stacked (inset in Fig. 4) and exhibit the characteristic pattern revealed by the subpixel correlation method (Fig. 1 and Milliner *et al.*, 2015). With regards to the stacked fault-parallel displacement, we measure the on-fault displacement by computing the displacement difference on the split nodes representing the fault (thick gray line in inset). The total displacement is measured by computing the difference of displacements

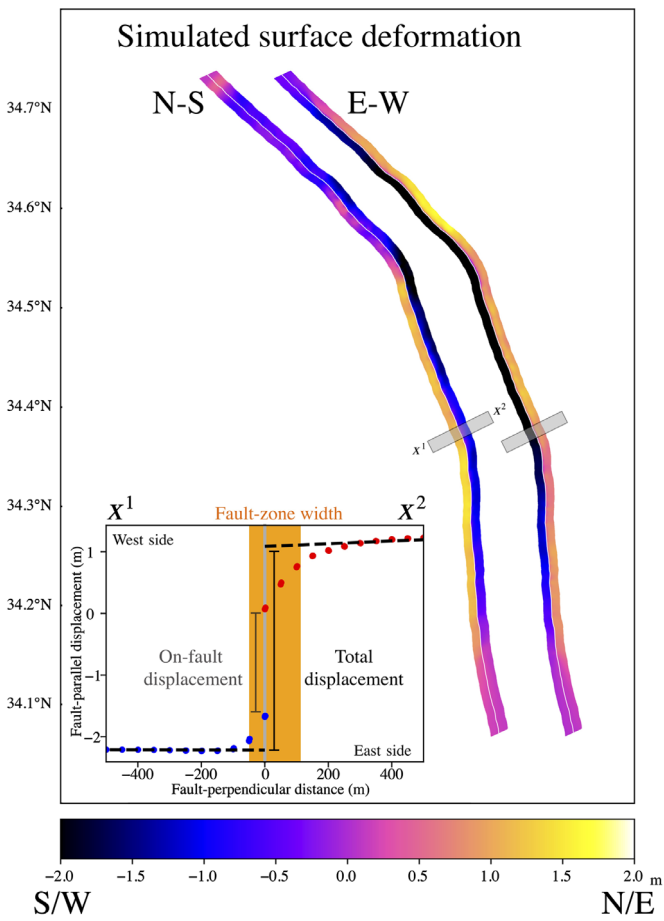
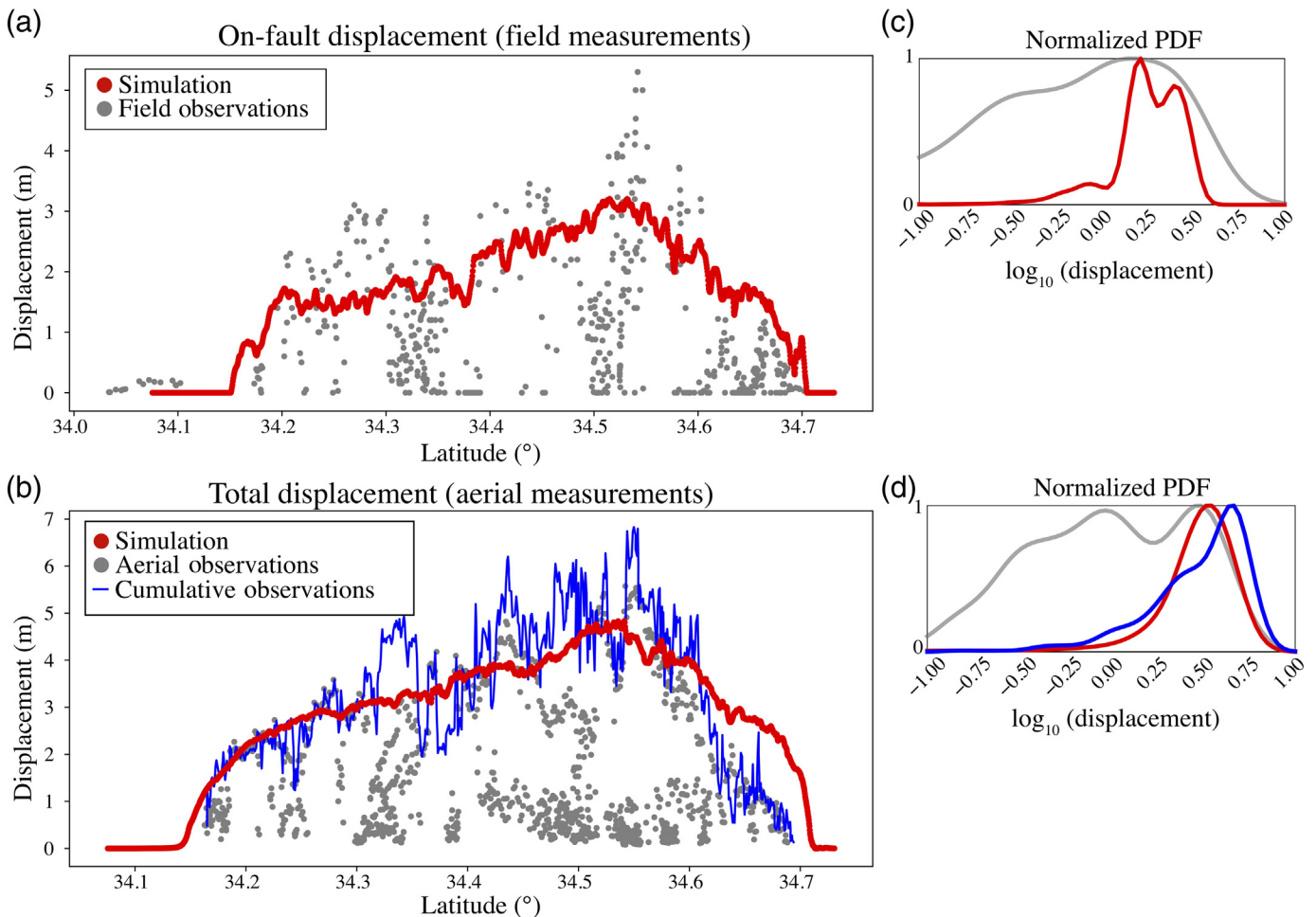


**Figure 4.** Simulated surface deformation and fault displacement from the preferred dynamic model. Two components of horizontal deformation within 3 km to the fault trace are plotted. A representative simulated fault displacement across the fault-perpendicular distance is shown in the inset figure where the total displacement, on-fault displacement, and fault-zone width (FZW) are defined. Dashed lines are the regression lines from the far-field deformations. E, east; N, north; S, south; W, west. The color version of this figure is available only in the electronic edition.

that are on-fault intercepts of lines best fitting the far-field deformations (>500 m off the fault) on each side. The FZW represents the fault-normal extent of observable surface shear in the form of smoothed transition of displacement (orange shaded box in the inset). Given that the stacked fault-parallel displacement is close to an error function shape, we define the FZW with a single number (and using a systematic approach that is repeatable) by fitting the normalized spatial derivative of fault-parallel displacement of each side with the derivative of an error function:  $\exp(-(x/a)^2)$  in which  $x$  is the distance to the fault, and  $a$  is the FZW. This approach, first published by Milliner et al. (2021), makes the definition of the FZW objective and reproducible, which is an advantage over previous estimates (e.g., Milliner et al., 2015). We estimate the on-fault displacement, total displacement, and FZW within each stacking window, thereafter

computing the corresponding OFD as the difference between the total and on-fault displacement. Finally, we compute the OFD ratio as the ratio between OFD and the total displacement, and compile all these metrics into a single dataset for follow-up analyses.

On-fault displacements of the preferred model and field measurements (as compiled in Sarmiento et al., 2019) are compared in Figure 5a. We observe a good agreement in the global spatial distribution of the peak displacements from both datasets near 34.5° latitude corresponding to the connection between the HVS and CREVS fault. This suggests that the orientations of the causative stress and faults have a first-order impact on the distribution of fault displacement. However, the along-strike variability of the field-derived fault displacement is much greater than that of the preferred model. The simulated fault is ruptured along a single continuous strand, in contrast to a multisegmented rupture pattern in the actual event (Figs. 1 and 5a). This comes from the simplifications in our model setup, which by design is not defined to replicate the complex patterns controlled in part by structural complexities (Milliner et al., 2015) and shallow fault discontinuities (Oglesby, 2020). Figure 5b compares the total displacement between the simulation and the aerial measurements (as compiled in Sarmiento et al., 2019). A cumulative displacement interpreted from aerial observations (Milliner et al., 2015) is also superimposed. Milliner et al. (2015) projected all displacement measurements distributed over a spatially complex area onto a single, regional representative fault trace and summed them up to construct the cumulative displacement distribution. This measure of the observed distributed fault displacements over an apparent single-strand fault trace is much easier to compare with our simulated fault displacements that are designed for a single-strand fault. The simulated total displacement generally fits the interpreted observation-based cumulative displacement well, but with a lower along-strike variability, as noted earlier. For a more quantitative comparison, we also compute normalized probability density functions (PDFs) of distributions of both simulated and observed displacements using a  $\log_{10}$  scale, and illustrate them in Figure 5c,d. These PDFs show that our preferred model simultaneously captures large-scale statistical features (i.e., shapes and mean values) of on-fault and total fault displacements but misses the small-scale characteristics. The missed small-scale fractures are not only numerically challenging to remedy but also an inevitable consequence of the intrinsic noise of the fault-displacement data that may come from measurements, near-surface nonlinear sediment behavior, or nonplanar geometry effect (C. Goulet et al., 2021). Shaw (2011) examined how differences in displacements vary with differences in location separation using seven events and found that the variability of displacements extrapolated to zero separation is approximately 1 m, providing a sense of scale for the noise level in observed fault displacements. The noise level was found uncorrelated with the magnitude, mechanism, or site location.

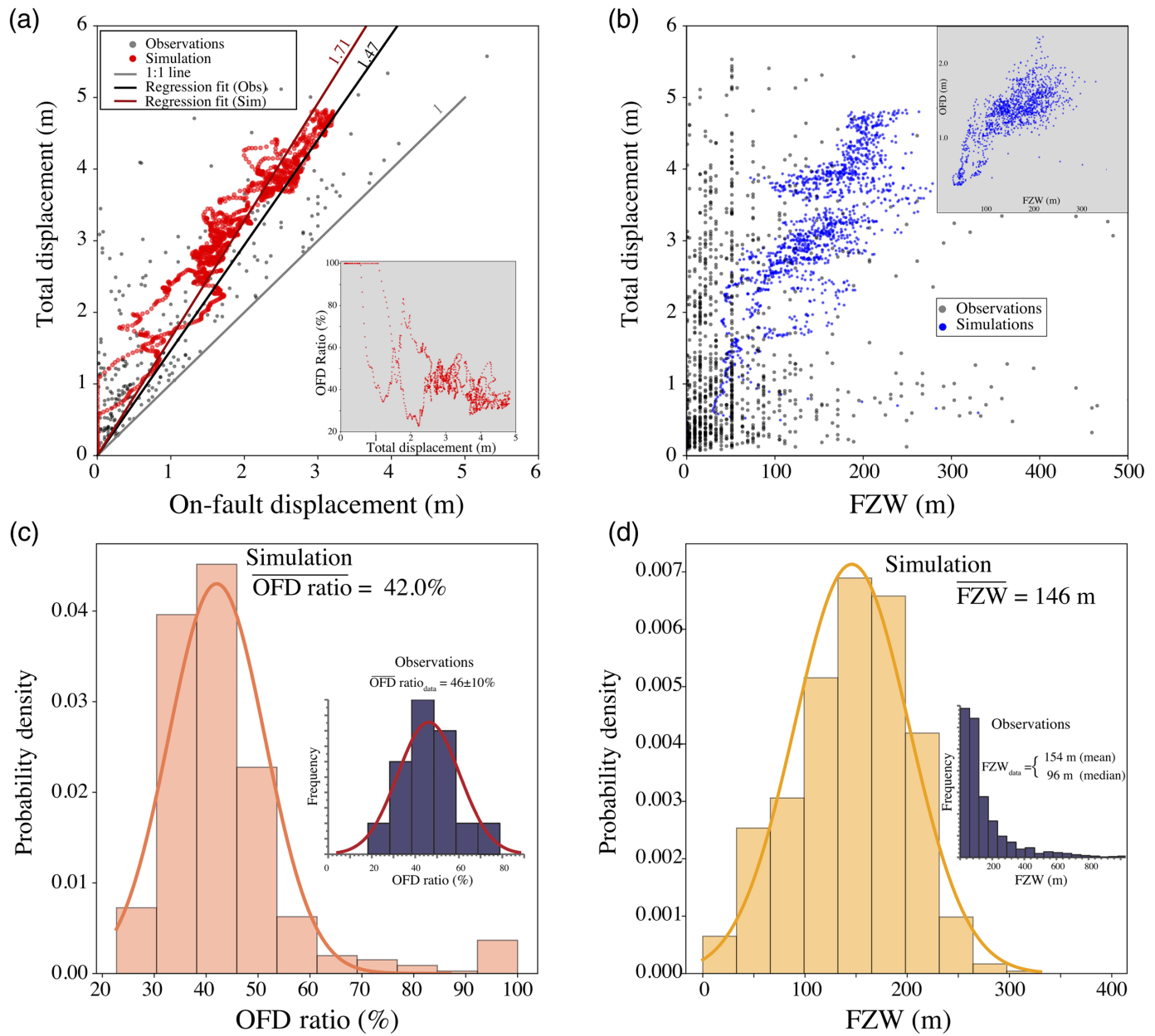


We find that the along-strike strain (the change in displacement per unit of along-strike distance) reflecting the extent to which the displacement varies along the strike is up to  $10^{-3}$  in the simulation; it is similar to that of observations of  $2 \times 10^{-3}$  in the Landers (Milliner *et al.*, 2015) and  $10^{-3}$  documented for other events (e.g., Michel and Avouac, 2006; Oglesby, 2008; Elliott *et al.*, 2009). Another metric representing the along-strike variability is the Hurst exponent of the power spectral density (PSD) of the fault displacement. The Hurst exponent of the simulated on-fault displacement is 0.63 (Fig. S2), which is close to that on the main rupture path from Landers ( $0.55 \pm 0.099$ ) and a modeling prediction ( $\sim 0.65$ ) based on a comparable roughness level, as Bruhat *et al.* (2020) documented. Figure S2 shows that the Hurst exponent of the on-fault displacement is smaller than that of the total displacement (0.88), implying that the on-fault variability is smoothed when a wider aperture in detection is applied. Nevertheless, the Hurst exponents of both on-fault and total displacement are systematically larger than that of the cumulative displacement (0.44; Milliner *et al.*, 2015), suggesting that the simulated geometrical fault roughness may be insufficient to represent the variability of a structurally complex event such as Landers, and that additional complexities

**Figure 5.** (a) Simulated on-fault displacement and comparison with field mapping. (b) Simulated total displacement and comparison with aerial mapping. A cumulative displacement from the aerial mapping (blue curve) is superimposed. Normalized probability density functions (PDFs) of observations and simulations in (a) and (b) are plotted in (c) and (d), respectively. The legends in (c) and (d) are consistent with those in (a) and (b). The color version of this figure is available only in the electronic edition.

(e.g., surrounding material and friction heterogeneity) may be needed in modeling to capture them (Bruhat *et al.*, 2020).

Figure 6a shows the partition of total and on-fault displacements at points along the fault. Both the simulations and observations indicate that considerable displacement occurs in the off-fault region (as indicated by the larger than 1 slope, from data regression), and that the trends are quite similar for both datasets, with the simulations exhibiting a larger slope. The simulated OFD ratio (inset in Fig. 6a) has a globally negative correlation with the total displacement. Such a correlation that the OFD ratio is lower in high-slip portions of ruptures has been reported for Landers (Milliner *et al.*, 2015) and for other recent earthquakes such as the 2010 El Mayor–Cucapah earthquake (Teran *et al.*, 2015) and the 2019 Ridgecrest Earthquake Sequence events (Gold *et al.*, 2021).



The shear-strain field can be important for certain engineering applications and can be approximated by the halved ratio between the total displacement and the FZW. In the simulation dataset, the total displacement is positively correlated with the FZW (Fig. 6b), and the average ratio of around  $2.5 \times 10^{-2}$  corresponds to a shear strain of  $\sim 1.3 \times 10^{-2}$  similar to that estimated from the aerial correlation map (Milliner et al., 2016). In addition, the OFD positive correlation with the FZW (inset in Fig. 6b) in the simulation is also consistent with observations in the Landers (Milliner et al., 2015) and Ridgecrest (Gold et al., 2021) events. However, the observed aerial dataset (gray dots in Fig. 6b) shows that the total displacements tend to be concentrated within a small FZW relative to the simulated dataset (blue dots in Fig. 6b), implying that significant localized shear strains due to very complex fault geometry are missed by the simulations.

**Figure 6.** Comparison of simulation results (preferred model, Sim.) for different displacement metrics against aerial observations (Obs), as interpreted by Milliner et al. (2015). (a) Correlation between the total and on-fault displacement from simulations and observations. (Inset) Correlation between off-fault deformation (OFD) ratio and total displacement of the preferred model. (b) Correlation between the total displacement and the fault-zone width (FZW) from simulations and observations. (c) Histograms of the simulated OFD ratio with inset showing that from observations. A fitted normal distribution (pink line) is superimposed. (d) Histogram of the simulated FZW with inset showing that from observations.

Statistical characteristics of the OFD ratio and FZW in the simulation dataset are plotted in Figure 6c,d. The simulated OFD ratio follows a normal distribution with a mean value of 42%, showing agreement with that of the aerial dataset. For the FZW, the simulation dataset nearly follows a normal

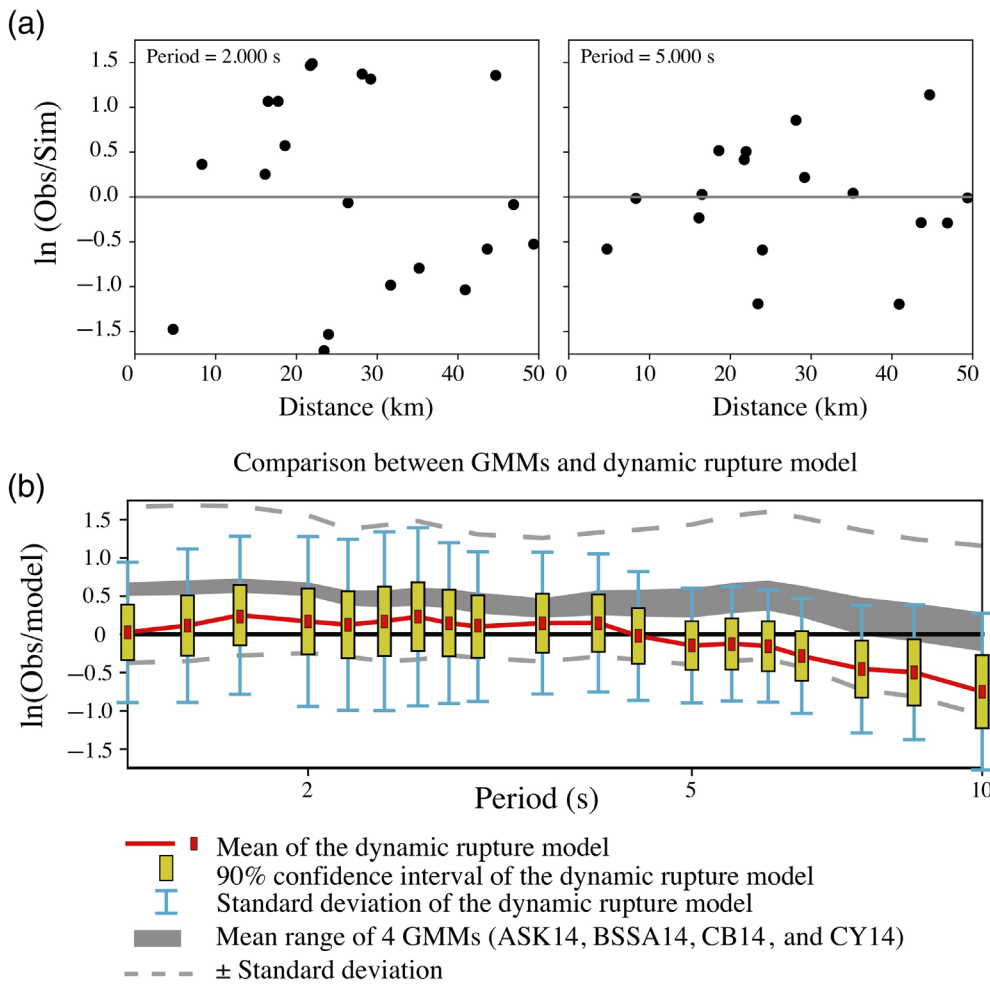


**Figure 7.** (a) Stationwise bias plots comparing 5% damped RotD50 ground motions between the simulations and observations at periods of 2 and 5 s. (b) Bias plots comparing results from the dynamic model against those of ground-motion models (GMMs; [Abrahamson et al., 2014](#) [ASK14]; [Boore et al., 2014](#) [BSSA14]; [Campbell and Bozorgnia, 2014](#) [CB14]; [Chiou and Youngs, 2014](#) [CY14]). The statistics of the GMMs and simulations are relative to the observation fit from all the stations. The red curve indicates the mean of the dynamic model, whereas the yellow boxes and blue bars represent the 90% confidence interval of the mean and the standard deviation centered around the mean, respectively. The gray shade is the range of mean residual of four GMMs, and dashed lines depict standard deviation of bias. The color version of this figure is available only in the electronic edition.

distribution as well with a mean value of 146 m close to the mean of the aerial dataset (154 m). However, the FZW from the aerial dataset distinctly follows an exponential distribution and contains a great number of small-scale ruptures that are missed in the dynamic model. Given our simplifying modeling assumptions, the impact of small-scale fractures or strands is not captured by the simulations. This is a compromise we have to contend with. A potential solution would be to filter the data below a certain resolution, something to be investigated once many scenarios have been validated. However, the FZW of other earthquakes may follow distinct distributions due to a change of tectonic settings. For instance, the 1999 Hector Mine earthquake is instead much closer to a normal distribution ([Milliner et al., 2016](#)).

We also perform a validation of simulated ground motions against recordings from the event to ensure that all physics important to modeling have been properly parameterized. The goal of this validation is, therefore, more a consistency check than a thorough validation and is based on pseudo-spectral acceleration (PSA), and not waveform comparisons. The locations of seismic stations are denoted by blue triangles on the map (Fig. 1) at which we simulate surface ground motions. We postprocess the simulated and observed ground motions using the SCEC BBP ([Maechling et al., 2015](#)) tools. The BBP computes relevant statistics from observation and simulation datasets, parameters needed for comparisons with empirical GMMs, and a goodness-of-fit (GOF) in terms of log residuals ( $\ln(\text{Obs}/\text{Sim})$ ). Figure 7a shows a stationwise comparison of 5% damped RotD50 PSA between the data and the simulation for periods of 2 and 5 s. Although data are limited, the mean GOF is near zero, the scatter is comparable to that from other studies (e.g., [Dreger et al., 2015](#)), and there is no systematic trend with distance. Figure 7b shows the same GOF metric against spectral period aggregated across all the stations. The figure includes a comparison of the GOF from our simulation and from an aggregate of four GMMs ([Abrahamson et al., 2014](#); [Boore et al., 2014](#); [Campbell and Bozorgnia, 2014](#); [Chiou and Youngs, 2014](#)). We find that the simulated ground motions produced by the dynamic model on average better match the observations relative to the GMMs, as the dynamic model inherently addresses the event-specific nature of Landers in terms of source and wave propagation. GMMs provide median global predictions of ground motions, with the between-event variability captured by an external event term (between-event residual). In addition, the dynamic model produces fit variability comparable to that from GMMs for a given observed earthquake. The dynamic rupture model overpredicts ground-motion periods beyond 5 s

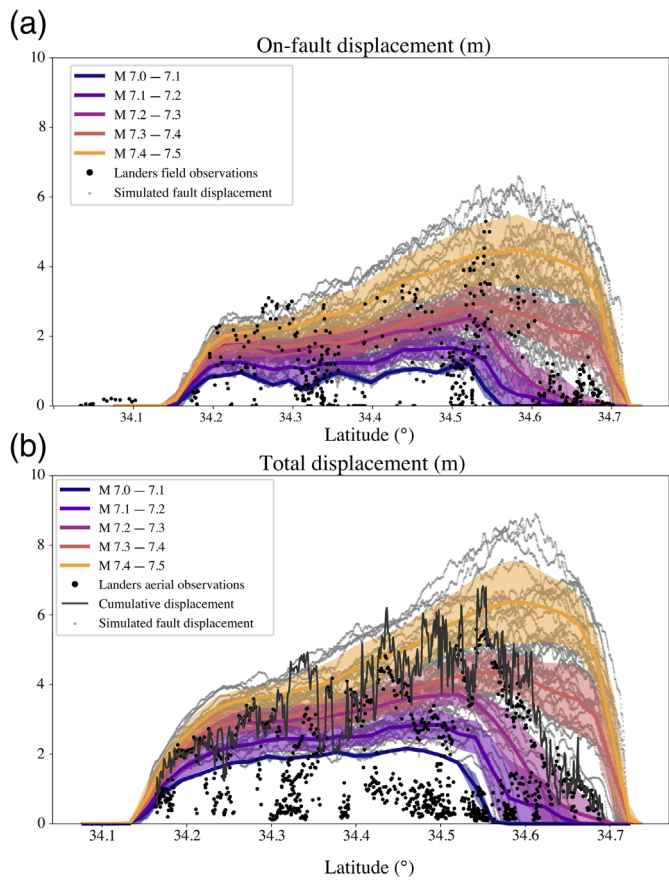


**Figure 8.** Simulated (a) on-fault and (b) total displacements from the suite of dynamic model simulations. The results are binned by magnitude with the mean (solid curves) and standard deviation (shaded areas) of displacements shown for each bin. Gray and black dots are simulated and observed displacements from Landers, respectively. The thin dark gray curve in (b) is the cumulative displacement interpreted from Landers aerial observations (identical to the blue curve shown in Fig. 5).

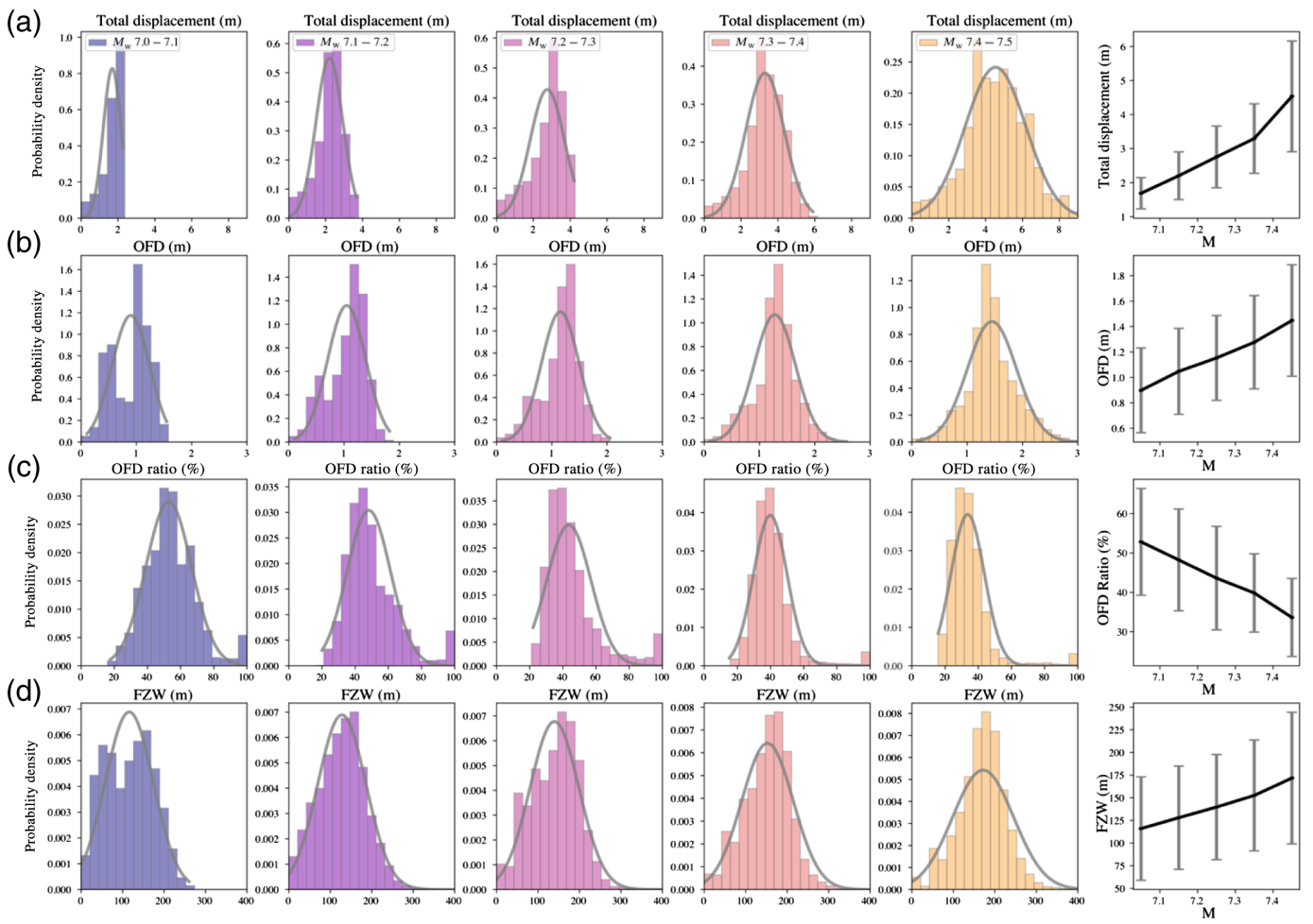
(Fig. 7b). This is likely due to the use of a 1D velocity model in which the S wavespeed at the shallow depth is as low as 550 m/s, systematically amplifying the simulated ground motions of stations located on the much stiffer structures in the north (Fig. S3). Another possible reason accounting for the long-period misfit is the relatively high stress drop used in our simulation. Considering the trade-off effect between the stress and plasticity model in generating the fault displacement, a lower stress drop along with a weaker rock strength may help resolve the long-period misfit while maintaining fault displacements that are observationally consistent. This is something we will consider in future simulations. On the other hand, such deviations from a GOF of zero are consistent with previous results (Dreger *et al.*, 2015) for ground motions simulated in a 1D-layered medium. Overall, the ground motions resulting from our preferred model are reasonable and confirm that the modeling assumptions are adequate and do not lead to unrealistic ground motions.

## Suite of predictive models

The development of PFDHA models requires that several datasets be available for the definition of a stable prediction of median and standard deviation of expected future displacement metrics. Simulations can supplement the empirical datasets, which are rarely as detailed and complete as for the Landers event. Our first set of such forward simulations are built using the model setup developed through the Landers validation. While preserving most input parameters of the dynamic model (e.g., fault length, friction properties, and rock materials), we relax fault roughness and on-fault stress conditions to capture modeling uncertainties, thus generating models with a wide range of resultant magnitudes. Specifically, we create 12 distinct, self-similar fault roughness realizations with roughness levels identical to that used in the preferred model and three additional stress conditions specified by a segment-varying  $R$  that accounts for the uncertainties of the stress amplitudes and orientations (See details in Table 1.). Consequently, a suite of 48 scenarios is simulated by iterating each roughness realization and stress condition. For analyzing the magnitude dependence of fault-displacement metrics, we divide all resulting scenarios into five bins based on their magnitudes from 7.0 to 7.5.

Figure 8 illustrates on-fault and total displacements of magnitude-binned dynamic models and from the Landers event. As the magnitude increases, the surface rupture length grows from about 40 to 70 km, which roughly follows the scaling between the surface rupture length and the magnitude predicted by Wells and Coppersmith (1994) except that at the high-magnitude end, because the rupture was originally bounded for the M 7.3 Landers event. Earthquakes with lower magnitudes tend to partially rupture the fault, as expected, and they terminate near the kink structure between the HVS and CREVS faults, which supports the plausible unfavorable bend argued in Wollherr *et al.* (2019). Once the kink is overcome and the CREVS segment begins to rupture, the peak displacement is found near the HVS and CREVS connection point or on CREVS as a consequence of the large angle of the CREVS relative to the maximum principal stress and the potentially large stress drop on CREVS. Although the surface rupture is rather complex, the first-order spatial pattern of displacement such as the zone of peak displacement could be controlled by the large-scale tectonic settings, for example, the orientations of fault and stress (in this study) or the fault maturity (Perrin *et al.*, 2016), which may lay a physical foundation for implementing additional predictive simulations.

The simulated total displacement is again systematically larger than the on-fault displacement in each magnitude bin, as shown in Figure 8. The extent to which the on-fault and total displacements are different will be discussed later. To test the predictivity of the ensemble models, we compare the amplitude and gradient of the binned simulated displacements with observations from the Landers event. Through this test, we find that Landers is closer to the scenarios with the magnitude



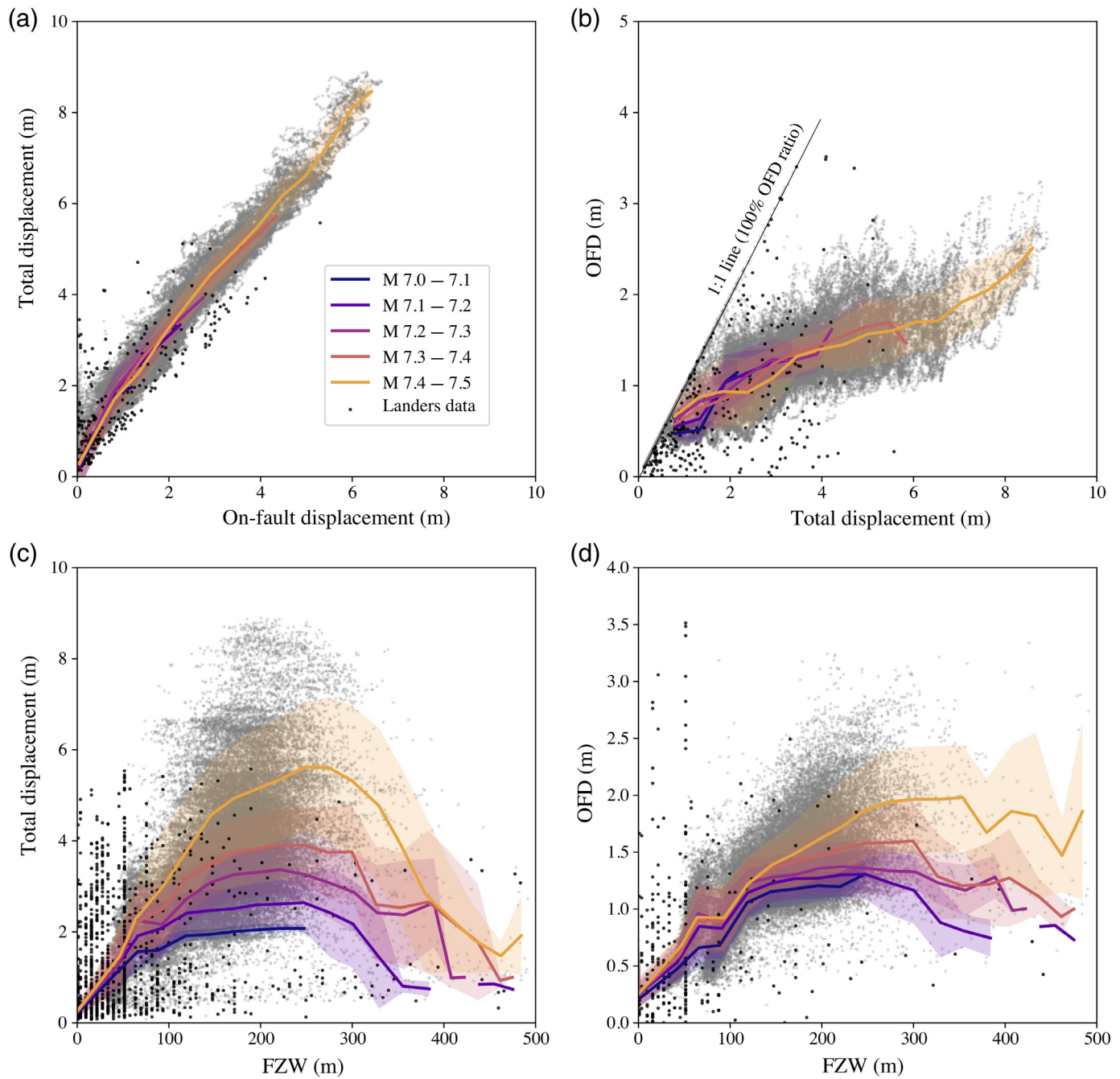
between 7.2 and 7.4 (violet and pink curves in Fig. 8b) enclosing the ground-truth (7.3) Landers magnitude. This test implies that the physics-based dynamic rupture model is not only likely to quantitatively address observationally consistent fault displacements but also able to simulate events with a wide magnitude range by capturing physically plausible uncertainties, to support the PFDHA model development.

Next, we present the histograms of total displacement, OFD, OFD ratio, and FZW of simulations within each magnitude bin with their mean values and standard deviations (Fig. 9). As seen with the preferred model, all these quantities approximately follow normal distributions. Although some of the histograms exhibit a certain level of skewness, we fit a normal distribution as a way to provide general trends in mean and standard deviation values. The rightmost column in Figure 9 aggregates those means and standard deviations as a function of magnitude. The ensemble models indicate that as the magnitude increases, total displacement, OFD, and FZW all increase, whereas the OFD ratio tends to decrease. The ensemble simulations centered on a magnitude of 7.3 slightly overpredict the total displacement and OFD relative to those (1.52 and 0.8 m) observed in Landers. This is consistent with the observations made in Figure 6, as these quantities

**Figure 9.** Histograms of (a) total displacement, (b) off-fault displacement (OFD), (c) OFD ratio, and (d) fault-zone width (FZW) within each magnitude bins. The magnitude-dependent mean and standard deviation determined by the normal distribution fit (gray thin curve in each bin) are plotted in the rightmost column. The color version of this figure is available only in the electronic edition.

in Landers follow an exponential distribution with an abundance of small-scale ruptures not modeled in our simulations. The decreased OFD ratio with increased magnitudes infers that surface deformation is more localized on the high-slip fault plane (large magnitude), which is widely supported by studies of the Landers (Milliner *et al.*, 2015), Hector Mine (Milliner *et al.*, 2016), El Mayor–Cucapah (Teran *et al.*, 2015), and Ridgecrest (Gold *et al.*, 2021) events. This result is also in agreement with the general geological findings that the extent of OFD is enhanced by structurally immature faults (Hollingsworth *et al.*, 2012; Dolan and Haravitch, 2014) and the notion that a mature fault is prone to bear larger magnitude earthquakes (Bletery *et al.*, 2016; Perrin *et al.*, 2016).

Figure 10 illustrates the correlations among the fault-displacement metrics and their dependencies on magnitudes. As seen in the observed dataset, the total displacement on average



increases with the OFD (Fig. 10a). The mean curves of total displacement show a subtle magnitude dependence and stay in a relatively narrow zone (around one standard deviation, the shaded area in Fig. 10a). A similar pattern is unveiled in the positive correlation between the OFD and the total displacement (Fig. 10b). In the Landers dataset, there are numerous data points very near the 1:1 line, highlighting that OFDs are identified, but little on-fault slip is observed (Fig. 10b) at certain locations along the fault. Similar examples of little or no discreet faulting but large distributed deformation have been observed in the 2005 M 6.5 Bam (Fialko *et al.*, 2005) and the 2010 Darfield (Van Dissen *et al.*, 2011) earthquakes. In contrast, correlations of the total displacement and OFD with the FZW show

**Figure 10.** Correlation relationships between (a) total and on-fault displacement, (b) off-fault displacement (OFD) and total displacement, (c) total displacement and fault-zone width (FZW), and (d) OFD and FZW within each magnitude bin for the suite of models. The mean and standard deviation are represented by the colored curve and shaded area for each bin. Background gray dots and foreground black dots are the simulation dataset and the Landers observations, respectively.

manifest magnitude dependencies (Fig. 10c,d). As the FZW approaches around 100 m, the total displacement and OFD monotonically increase with the FZW (inelastic deformation is limited in this phase). Then, both present an approximate

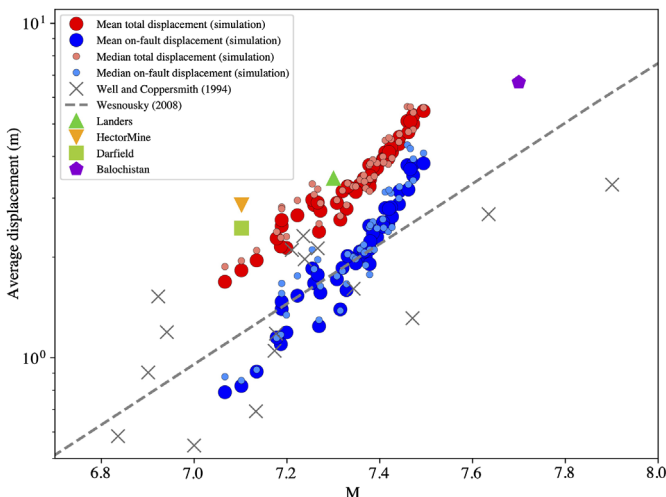


**Figure 11.** Scaling relationship of mean displacement with magnitude for simulated and recorded strike-slip earthquakes. Red and blue circles represent the mean values of the total and on-fault displacements from the suite of simulations, whereas light red and blue circles represent the corresponding median values. Crosses show the data included in Wells and Coppersmith (1994). The dashed line is the power-law regression of the mean displacement from Wesnousky (2008). Four data points of the mean displacements aerially estimated (Landers, Hector Mine, Darfield, and Balochistan earthquakes) are superimposed. The color version of this figure is available only in the electronic edition.

saturation over the FZW from 100 to 300 m and then tend to taper to a larger FZW. The magnitude-dependent saturation is a consequence of the yielding effects caused by the implemented off-fault plasticity, which is also found to saturate near-fault ground motions and directivity amplification (Wang and Day, 2020). A similar saturation pattern of total displacement near 1 and 3 m is noted in the Landers dataset (Fig. 10c). The reduced total displacement above the FZW of  $\sim 300$  m is attributed to the large FZW mostly found at the rupture terminations or structurally complex segments in which the total displacement is generally small.

Scaling laws relating mean displacement to magnitude are an essential component of PFDHA models (e.g., Petersen *et al.*, 2011; Field *et al.*, 2014). Provided that the recently observed total fault displacements from the aerial mapping are systematically greater than those from the field mapping, preexisting scaling relation such as Wells and Coppersmith, 1994 miss the OFD and may lead to a significant bias of fault-displacement hazard. As shown in Figure 11, the mean values of total displacements in the 1992 Landers (3.41 m in Milliner *et al.*, 2016), 1999 Hector Mine (2.84 m in Milliner *et al.*, 2016), 2010 Darfield ( $\sim 2.5$  m in Quigley *et al.*, 2012), and 2013 Balochistan ( $\sim 8$  m in Zinke *et al.*, 2014) earthquakes are systematically larger than those predicted by empirical models (Wells and Coppersmith, 1994; Wesnousky, 2008). However, thus far, fault-displacement datasets containing aerially derived total displacements are too sparse to be built upon. This is one area for which simulations can supplement

the empirical datasets. We compute the mean and median displacement of on-fault and total displacement for our suite of models and plot them in Figure 11. The simulated on-fault displacements (mean and median) are within the empirical prediction range, and the simulated total displacements are consistent with the limited COSI-Corr observations. This comparison suggests that the dynamic rupture method has the capability to capture observation-consistent characteristics of both on-fault and total displacements. The steepening of the slope beyond M 7.3 comes from the fault length being fixed for the original Landers scenario. Extending the model so that it can accommodate larger areas will change that relationship, and this is something we will investigate in future work.

## DISCUSSION

In this study, we developed a dynamic rupture model that leads to simulated fault displacement metrics consistent with those observed from the 1992 Landers earthquake. However, when compared with the detailed fault-displacement observations, two major discrepancies are emergent. The first is that our simplified dynamic rupture simulations substantially overlook the small-scale fault displacements, as represented by the exponential distributions of the total displacement, OFD, and FZW. These small-scale observations may have significant implications on the mechanisms of surface rupture and OFD but are physically and computationally challenging to model. The second discrepancy is that the simulated along-strike variability useful for constructing PFDHA models (Lavrentiadis and Abrahamson, 2019) is systematically lower than that of the observation dataset. As an indicator, the slopes or Hurst exponents obtained from numerical simulations are often overestimated. It is a likely consequence of the model simplification without considering other controls on displacement heterogeneity. We prioritized the modeling of the intermediate-to-large scale features of fault displacements. We also note that part of these discrepancies may also be due in part to how the observational data are interpreted. Given that datasets collected from either field or aerial mapping are sampled as a data cloud, a strike-variable fault displacement used for evaluating the spectral signatures is subjectively created, for example, by selecting a major rupture path (Bruhat *et al.*, 2020), cumulating projected data back to a fault line (Milliner *et al.*, 2015), or integrating the local maximum fault displacements over distance bins (Gold *et al.*, 2021). The interpretation of imagery is also potentially affected by pixel color and saturation, which may lead to an overprediction of displacements near the pixel resolution (C. Goulet *et al.*, 2021). These subjective processes may lead to distinct evaluations for the same event or dataset. For instance, Bruhat *et al.* (2020) and Milliner *et al.* (2015) use different methods to obtain distinct spectral signals (i.e., PSD) for the Landers earthquake and obtain different results. This type of difference should be quantified as part of the interpretation uncertainty.

The dynamic rupture model is explicitly site-specific. That is, the predicted variability in fault displacements at a given site inherently includes all the characteristics of the 3D fault and surrounding material specific and unique to that site. To broaden the applicability and enhance the predictivity of dynamic rupture models for future site-specific events, the uncertainties of the modeling approach and input parameters have to be appropriately addressed in the physics-based modeling. By generalizing our simulation set, we make it more broadly usable to inform the scaling of displacements with different ingredient characteristics, making them more broadly usable to support PFDHA development. We expect that our future work including additional scenarios will allow us to set better bounds on the parameter space to sample to capture more of the California events. As we develop new rupture models spanning different geometries, fault mechanisms, and stress fields, we will refine and most likely expand that parameter space so that it is consistent with several past events. We are also considering expanding our modeling to include brittle damage as an improvement over to the plasticity model described here. Although others have successfully used damage mechanics in the dynamic rupture model (e.g., Yamashita, 2000; Dalguer *et al.*, 2003; Bhat *et al.*, 2012; Lyakhovsky and Ben-Zion, 2014; Thomas and Bhat, 2018), we plan to evaluate an implementation to investigate its impact on displacement modeling. And although both types of models limit stress at high strain, a key difference is that the brittle damage changes the elastic moduli of the host rock whereas plasticity does not. Thus, the resultant low-velocity zone widely documented in the field may impact the distribution of peak fault displacement (Cappa *et al.*, 2014) and spatial extent of the FZW (Roten *et al.*, 2017). Specifically, the microfracture-based brittle damage model in Thomas and Bhat (2018) may support modeling of the currently missed small-scale surface ruptures.

We summarize below the need for continued work in related fields of study that will support the dynamic rupture modeling input for the PFDHA. The continued improvement in these fields will impact the selection of input parameters for key ingredients, even for simplified models such as ours.

- Fault mapping:** Consistently mapping principal and secondary fault traces is a basis of PFDHA to address the potential fault-displacement hazard. The postearthquake exhaustive reconnaissance mapping of coseismically ruptured faults is valuable for supporting validation (e.g., Ponti *et al.*, 2020; C. Goulet *et al.*, 2021). Furthermore, the prerupture fault mapping from geomorphology (e.g., Arrowsmith and Zielke, 2009) and its comparison with the postevent fault rupture data may provide clues about seismic hazards and issues related to the repeatability of specific rupture geometries on the surface. Both types of fault mapping are beneficial to construct site-specific dynamic rupture models.

- Fault history:** The fault history revealed from paleoseismic trenching and geomorphological surveys can also support the development of more appropriate dynamic rupture models. As stated in Milliner *et al.* (2015) and Hollingsworth *et al.* (2012), the OFD and FZW are controlled by the fault maturity represented by the cumulative slip, which can provide insight into how much OFD will be accommodated in future earthquakes. The inferred fault maturity can then provide constraints on the level of fault roughness to implement to appropriately reproduce the desired along-strike displacement variability and/or high-frequency ground motion (Shi and Day, 2013). In our dynamic rupture models, the structural controls shown in Figure S5 impacted the modeling decision, in which the large OFD ratio and FZW occur in the framed segments of either a big change in strike angle or with the rupture termination. In addition, a detailed segmented fault history could be used to constrain fault and stress properties. For example, the cyclicity (e.g., periodic cycle or supercycle) revealed from paleoseismic studies may provide insight on the buried fault structure, the interseismic stress transfer mode, and the degree of fault segment coupling (Scharer *et al.*, 2017; Philibosian and Meltzner, 2020). For a periodic paleoseismic record on a certain segment of the fault, a long recurrence period accompanied with dominantly large-magnitude events would imply higher friction if the paleoseimicity shows a more regular moderate magnitude stress release (e.g., Dal Zilio *et al.*, 2019). Hence, continued work on such paleoseismic studies is important and can provide useful constraints for rupture modeling.

- Stress condition:** The stress condition is another poorly constrained parameter. It is temporally and spatially variable, as it evolves with tectonic processes and multiphase interplay (e.g., fluid transportation). Relative to its magnitude, the orientation of the stress field is less challenging to be constrained, and, as seen in our study, the orientations of fault and stress synergistically make a first-order impact on the fault displacement (e.g., peak displacement location). Close monitoring of regional seismicity and stress orientation from geodetic transients offers an opportunity to address a variability caused by the in situ stress in the physics-based modeling framework. The SCEC Community Stress Model (e.g., Bird, 2017) is one such effort that constructs a suite of models and constraints on the stress and stress rate in the southern California lithosphere.

- Rheology of surface material:** The rheology of surface materials impacts the relative amount of OFD for a given total displacement. The OFD was found to be large in areas of younger sediments (Oskin *et al.*, 2012; Quigley *et al.*, 2012; Milliner *et al.*, 2016), but this relationship does not always appear consistent (Milliner *et al.*, 2015; Gold *et al.*, 2021). Understanding this complex pattern deserves continued theoretical and observational studies, especially for the more complicated circumstance in which the deformation

occurs at sites of sediment–bedrock interfaces. In our current model, we use the 1D-layered velocity structure for simplicity, but dynamic rupture models capable of enabling the heterogeneous and bimaterial complexity will be developed for understanding and predicting the distributed OFD in such complex settings.

## CONCLUSION

Coseismic fault displacements in large earthquakes have caused significant damage to structures and lifelines near faults and impacted structural design and legislation over the years. Unlike well-developed GMMs, empirical fault-displacement models are sparse and poorly constrained partly due to the paucity of detailed fault-displacement observations. The physics-based dynamic rupture model has the potential to address this limitation. The overarching goal of this study was to develop and validate the dynamic rupture model so that it can reproduce observed fault displacements from past events and serve to generate datasets for yet unobserved events. We focused this initial study by calibrating and validating the dynamic rupture model with the 1992 M 7.3 Landers earthquake. Our validation and forward simulation exercise included (1) the definition of a preferred dynamic rupture model that systematically reproduces the first-order metrics of the fault displacement (such as the total displacement, the mean OFD ratio, the mean FZW, and the location of the peak displacement) and (2) the development of a suite of dynamic rupture models quantifying expected fault-displacement metrics, their scaling, and magnitude dependencies that are in part supported by Landers and other recent earthquakes.

Through these validations, we demonstrate that the dynamic rupture model has a promising potential to develop physics-based fault-displacement datasets that alone or combined with empirical observations can support PFDHA models. Furthermore, dynamic rupture models recently make a push to extend deterministic ground-motion simulations to higher frequencies used for engineering applications (e.g., Andrews and Ma, 2016; Withers *et al.*, 2019), further extending their potential use for engineering applications. Our validation study highlights that the dynamic rupture model can provide defensible forward simulations for both ground-motion and fault-displacement hazards, serving communities of PSHA and PFDHA development. Encouraged by this validation exercise, more scenarios and events will be implemented with a similar approach to validate the dynamic rupture model, and to include other strike-slip events (e.g., the M 7.1 Hector Mine and the M 7.1 Ridgecrest earthquakes), reverse mechanism events (e.g., M 7.7 Chi-Chi earthquake), and events of relatively small magnitudes (M 6–7, e.g., the M 6.4 Ridgecrest earthquake). Continuing with well-documented events, as listed previously, is the next logical step. However, once we have built better constraints, we would also like to revisit poorly documented events and fill the data gaps on a per-event basis.

## DATA AND RESOURCES

The open-source software package Support Operator Rupture Dynamics (SORD) can be downloaded from <https://github.com/wangyf/sordw3>. We cite the Fault Displacement Hazard Initiative (FDHI) dataset that is still under development (<https://www.risksciences.ucla.edu/nhr3/fdhi/databases>). The ground-motion validation was performed using the Broadband Platform (BBP; <https://github.com/SCECcode/bbp>). Figures in this article were prepared using Paraview (<https://www.paraview.org/>) and Matplotlib (<https://matplotlib.org/>). All websites were last accessed in February 2021. The supplement material contains five figures showing details of model development and simulation results.

## DECLARATION OF COMPETING INTERESTS

The authors acknowledge that there are no conflicts of interest recorded.

## ACKNOWLEDGMENTS

This work was supported in part by the California Energy Commission and the Pacific Gas and Electric Company. Additional support was provided by the Southern California Earthquake Center (SCEC, Contribution Number 10961). SCEC is funded by the National Science Foundation (NSF) and the U.S. Geological Survey (USGS) through cooperative agreements with the University of Southern California (USC). The authors would like to thank Yousef Bozorgnia, Luis Dalguer, Albert Kottke, Greg Lavrentiadis, Chris Milliner, Rob Moss, Alex Sarmiento, Steve Thompson, and Bob Youngs for their valuable suggestions. Simulations for this research were performed on the Frontera system at the Texas Advanced Computing Center (TACC) through the Large-Scale Community Partnerships (LSCP) allocation program and on Theta at the Argonne Leadership Computing Facility (ALCF) under Contract DE-AC02-06CH11357, through the U.S. Department of Energy (DOE) Innovative and Novel Computational Impact on Theory and Experiment (INCITE) program. Finally, the authors would like to thank the BSSA Special Section Guest Editor Rui Chen, Editor-in-Chief Thomas Pratt, and the two anonymous reviewers who helped improve this article.

## REFERENCES

- Abrahamson, N. A., W. J. Silva, and R. Kamai (2014). Summary of the ASK14 ground motion relation for active crustal regions, *Earthq. Spectra* **30**, 1025–1055.
- Andrews, D. J., and S. Ma (2016). Validating a dynamic earthquake model to produce realistic ground motion, *Bull. Seismol. Soc. Am.* **106**, 665–672.
- Aochi, H., R. Madariaga, and E. Fukuyama (2003). Constraint of fault parameters inferred from nonplanar fault modeling, *Geochem. Geophys. Geosys.* **4**, doi: [10.1029/2001GC000207](https://doi.org/10.1029/2001GC000207).
- Arrowsmith, J. R., and O. Zielke (2009). Tectonic geomorphology of the San Andreas fault zone from high resolution topography: An example from the Cholame segment, *Geomorphology* **113**, 70–81.
- Baize, S., F. Nurminen, A. Sarmiento, T. Dawson, M. Takao, O. Scotti, T. Azuma, P. Boncio, J. Champenois, F. R. Cinti, *et al.* (2020). A worldwide and unified database of surface ruptures (SURE) for fault displacement hazard analyses, *Seismol. Res. Lett.* **91**, 499–520.
- Bhat, H. S., A. J. Rosakis, and C. G. Sammis (2012). A micromechanics based constitutive model for brittle failure at high strain rates, *J. Appl. Mech.* **79**, doi: [10.1115/1.4005897](https://doi.org/10.1115/1.4005897).

- Bird, P. (2017). Stress field models from Maxwell stress functions: Southern California, *Geophys. J. Int.* **210**, 951–963.
- Bletry, Q., A. M. Thomas, A. W. Rempel, L. Karlstrom, A. Sladen, and L. De Barros (2016). Mega-earthquakes rupture flat mega-thrusts, *Science* **354**, 1027–1031.
- Boore, D. M., J. P. Stewart, E. Seyhan, and G. M. Atkinson (2014). NGA-West2 equations for predicting PGA, PGV, and 5% damped PSA for shallow crustal earthquakes, *Earthq. Spectra* **30**, 1057–1085.
- Bouchon, M., M. Campillo, and F. Cotton (1998). Stress field associated with the rupture of the 1992 Landers, California, earthquake and its implications concerning the fault strength at the onset of the earthquake, *J. Geophys. Res.* **103**, 21,091–21,097, doi: [10.1029/98jb01982](https://doi.org/10.1029/98jb01982).
- Bozorgnia, Y., N. Abrahamson, B. Arcos, S. Baize, P. Boncio, S. Chao, R. Chen, B. Chiou, T. Dawson, J. Donahue, et al. (2021). An overview of the fault displacement hazard initiative research program, Presentation at the 2021 Annual Meeting of the Seismological Society of America, 19–23 April 2021, Online event.
- Bruhat, L., Y. Klinger, A. Vallage, and E. M. Dunham (2020). Influence of fault roughness on surface displacement: From numerical simulations to coseismic slip distributions, *Geophys. J. Int.* **220**, 1857–1877.
- Brune, J. N., and A. Anooshehpoor (1998). A physical model of the effect of a shallow weak layer on strong ground motion for strike-slip ruptures, *Bull. Seismol. Soc. Am.* **88**, 1070–1078.
- California Geological Survey (CGS) (2018). Earthquake fault zones—A guide for assessing fault rupture hazards in California, *Spec. Publ.* **42**, 83 pp.
- Campbell, K. W., and Y. Bozorgnia (2014). NGA-West2 ground motion model for the average horizontal components of PGA, PGV, and 5% damped linear acceleration response spectra, *Earthq. Spectra* **30**, 1087–1115.
- Cappa, F., C. Perrin, I. Manighetti, and E. Delor (2014). Off-fault long-term damage: A condition to account for generic, triangular earthquake slip profiles, *Geochem. Geophys. Geosys.* **15**, 1476–1493.
- Chen, R., and M. D. Petersen (2019). Improved implementation of rupture location uncertainty in fault displacement hazard assessment, *Bull. Seismol. Soc. Am.* **109**, 2132–2137.
- Chester, F., J. S. Chester, D. Kirschner, S. Schulz, and J. Evans (2004). Structure of large-displacement, strike-slip fault zones in the brittle continental crust, in *Rheology and Deformation of the Lithosphere at Continental Margins*, G. Karner, B. Taylor, N. Driscoll, and D. Kohlstedt (Editor), Columbia University Press, doi: [10.7312/karn12738-009](https://doi.org/10.7312/karn12738-009).
- Chiou, B. S. J., and R. R. Youngs (2014). Update of the Chiou and Youngs NGA model for the average horizontal component of peak ground motion and response spectra, *Earthq. Spectra* **30**, 1117–1153.
- Cohee, B. P., and G. C. Beroza (1994). Slip distribution of the 1992 Landers earthquake and its implications for earthquake source mechanics, *Bull. Seismol. Soc. Am.* **84**, 692–712.
- Cotton, F., and M. Campillo (1995). Frequency-domain inversion of strong motions—Application to the 1992 Landers earthquake, *J. Geophys. Res.* **100**, 3961–3975.
- Dalguer, L. A., K. Irikura, and J. D. Riera (2003). Generation of new cracks accompanied by the dynamic shear rupture propagation of the 2000 Tottori (Japan) earthquake, *Bull. Seismol. Soc. Am.* **93**, 2236–2252.
- Dalguer, L. A., H. Wu, Y. Matsumoto, K. Irikura, T. Takahama, and M. Tonagi (2019). Development of dynamic asperity models to predict surface fault displacement caused by earthquakes, *Pure Appl. Geophys.* **177**, 1983–2006.
- Dal Zilio, L., Y. van Dinther, T. Gerya, and J. P. Avouac (2019). Bimodal seismicity in the Himalaya controlled by fault friction and geometry, *Nat. Comm.* **10**, doi: [10.1038/s41467-018-07874-8](https://doi.org/10.1038/s41467-018-07874-8).
- Day, S. M., and G. P. Ely (2002). Effect of a shallow weak zone on fault rupture: Numerical simulation of scale-model experiments, *Bull. Seismol. Soc. Am.* **92**, 3022–3041.
- Day, S. M., L. A. Dalguer, N. Lapusta, and Y. Liu (2005). Comparison of finite difference and boundary integral solutions to three-dimensional spontaneous rupture, *J. Geophys. Res.* **110**, doi: [10.1029/2005JB003813](https://doi.org/10.1029/2005JB003813).
- Day, S. M., R. Graves, J. Bielak, D. Dreger, S. Larsen, K. B. Olsen, A. Pitarka, and L. Ramirez-Guzman (2008). Model for basin effects on long-period response spectra in southern California, *Earthq. Spectra* **24**, 257–277.
- Day, S. M., G. Yu, and D. J. Wald (1998). Dynamic stress changes during earthquake rupture, *Bull. Seismol. Soc. Am.* **88**, 512–522.
- Dolan, J. F., and B. Haravitch (2014). How well do surface slip measurements track slip at depth in large strike-slip earthquakes? The importance of fault structural maturity in controlling on-fault slip versus off-fault surface deformation, *Earth Planet. Sci. Lett.* **388**, 38–47.
- Donahue, J. L., and N. A. Abrahamson (2014). Simulation-based hanging wall effects, *Earthq. Spectra* **30**, 1269–1284.
- Dreger, D. S., G. C. Beroza, S. M. Day, C. A. Goulet, T. H. Jordan, P. A. Spudich, and J. P. Stewart (2015). Validation of the SCEC broadband platform V14.3 simulation methods using pseudospectral acceleration data, *Seismol. Res. Lett.* **86**, 39–47.
- Drucker, D. C., and W. Prager (1952). Soil mechanics and plastic analysis or limit design, *Q. Appl. Math.* **10**, 157–165.
- Elliott, A. J., J. F. Dolan, and D. D. Oglesby (2009). Evidence from coseismic slip gradients for dynamic control on rupture propagation and arrest through stepovers, *J. Geophys. Res.* **114**, doi: [10.1029/2008JB005969](https://doi.org/10.1029/2008JB005969).
- Ely, G. P., S. M. Day, and J.-B. Minster (2009). A support-operator method for 3-D rupture dynamics, *Geophys. J. Int.* **177**, 1140–1150.
- Fialko, Y. (2004). Probing the mechanical properties of seismically active crust with space geodesy: Study of the coseismic deformation due to the 1992  $M_w$  7.3 Landers (southern California) earthquake, *J. Geophys. Res.* **109**, doi: [10.1029/2003JB002756](https://doi.org/10.1029/2003JB002756).
- Fialko, Y., D. Sandwell, M. Simons, and P. Rosen (2005). Three-dimensional deformation caused by the Bam, Iran, earthquake and the origin of shallow slip deficit, *Nature* **435**, 295–299.
- Field, E. H., R. J. Arrowsmith, G. P. Biasi, P. Bird, T. E. Dawson, K. R. Felzer, D. D. Jackson, K. M. Johnson, T. H. Jordan, C. Madden, et al. (2014). Uniform California Earthquake Rupture Forecast, version 3 (UCERF3)—The time-independent model, *Bull. Seismol. Soc. Am.* **104**, 1122–1180.
- Gold, R. D., C. B. DuRoss, and W. D. Barnhart (2021). Coseismic surface displacement in the 2019 Ridgecrest earthquakes: Comparison of field measurements and optical image correlation results, *Geochem. Geophys. Geosys.* **22**, e2020GC009326, doi: [10.1029/2020GC009326](https://doi.org/10.1029/2020GC009326).
- Goulet, C., Y. Wang, C. C. Nweke, B. Tang, P. Wang, K. S. Hudson, S. K. Andi, X. Meng, M. B. Hudson, A. Donnellan, et al. (2021).

- Comparison of near-fault displacement interpretations from field and aerial data for the M 6.5 and 7.1 ridgecrest earthquake sequence ruptures, *Bull. Seismol. Soc. Am.* 1–17, doi: [10.1785/0120200222](https://doi.org/10.1785/0120200222).
- Goulet, C. A., N. A. Abrahamson, P. G. Somerville, and K. E. Wooddell (2015). The SCEC broadband platform validation exercise: Methodology for code validation in the context of seismic-hazard analyses, *Seismol. Res. Lett.* **86**, 17–26.
- Goulet, C. A., Y. Bozorgnia, N. Kuehn, L. Al Atik, R. R. Youngs, R. W. Graves, and G. M. Atkinson (2021). NGA-East ground-motion characterization model Part I: Summary of products and model development, *Earthq. Spectra* **37**, 1231–1282, doi: [10.1177/87552930211018723](https://doi.org/10.1177/87552930211018723).
- Gross, S., and C. Kisslinger (1997). Estimating tectonic stress rate and state with Landers aftershocks, *J. Geophys. Res.* **102**, 7603–7612.
- Harris, R. A., M. Barall, B. Aagaard, S. Ma, D. Roten, K. Olsen, B. C. Duan, D. Y. Liu, B. Luo, K. C. Bai, et al. (2018). A suite of exercises for verifying dynamic earthquake rupture codes, *Seismol. Res. Lett.* **89**, 1146–1162.
- Harris, R. A., M. Barall, R. Archuleta, E. Dunham, B. Aagaard, J. P. Ampuero, H. Bhat, V. Cruz-Atienza, L. Dalguer, P. Dawson, et al. (2009). The SCEC/USGS dynamic earthquake rupture code verification exercise, *Seismol. Res. Lett.* **80**, 119–126.
- Hoek, E., C. Carranza-Torres, and B. Corkum (2002). Hoek-Brown failure criterion—2002 edition, *Proc. of NARMS-Tac*, Vol. 1, edited, 267–273.
- Hollingsworth, J., J. F. Dolan, C. W. Milliner, S. Leprince, F. Ayoub, and J. Avouac (2012). Analysis of the shallow slip deficit using sub-pixel image correlation: Implications for fault slip rates, and seismic hazards, edited, T23H-02.
- Ida, Y. (1972). Cohesive force across tip of a longitudinal-shear crack and griffiths specific surface-energy, *J. Geophys. Res.* **77**, 3796–3805.
- Kaneko, Y., and Y. Fialko (2011). Shallow slip deficit due to large strike-slip earthquakes in dynamic rupture simulations with elasto-plastic off-fault response, *Geophys. J. Int.* **186**, 1389–1403.
- Kaneko, Y., N. Lapusta, and J. P. Ampuero (2008). Spectral element modeling of spontaneous earthquake rupture on rate and state faults: Effect of velocity-strengthening friction at shallow depths, *J. Geophys. Res.* **113**, doi: [10.1029/2007JB005553](https://doi.org/10.1029/2007JB005553).
- Lavrentiadis, G., and N. Abrahamson (2019). Generation of surface-slip profiles in the wavenumber domain, *Bull. Seismol. Soc. Am.* **109**, 888–907.
- Lindsey, E. O., Y. Fialko, Y. Bock, D. T. Sandwell, and R. Bilham (2014). Localized and distributed creep along the southern San Andreas fault, *J. Geophys. Res.* **119**, 7909–7922.
- Liu, J., K. Sieh, and E. Hauksson (2003). A structural interpretation of the aftershock “Cloud” of the 1992  $M_w$  7.3 Landers earthquake, *Bull. Seismol. Soc. Am.* **93**, 1333–1344.
- Lyakhovsky, V., and Y. Ben-Zion (2014). A continuum damage-breakage faulting model and solid-granular transitions, *Pure. Appl. Geophys.* **171**, 3099–3123.
- Maechling, P. J., F. Silva, S. Callaghan, and T. H. Jordan (2015). SCEC broadband platform: System architecture and software implementation, *Seismol. Res. Lett.* **86**, 27–38.
- Marinos, V., P. Marinos, and E. Hoek (2005). The geological strength index: Applications and limitations, *Bull. Eng. Geol. Environ.* **64**, 55–65.
- Marone, C. (1998). Laboratory-derived friction laws and their application to seismic faulting, *Annu. Rev. Earth Planet Sci.* **26**, 643–696.
- Michel, R., and J. P. Avouac (2006). Coseismic surface deformation from air photos: The Kickapoo step over in the 1992 Landers rupture, *J. Geophys. Res.* **111**, doi: [10.1029/2005JB003776](https://doi.org/10.1029/2005JB003776).
- Milliner, C., A. Donnellan, S. Aati, J.-P. Avouac, R. Zinke, J. F. Dolan, K. Wang, and R. Bürgmann (2021). Bookshelf kinematics and the effect of dilatation on fault zone inelastic deformation: Examples from optical image correlation measurements of the 2019 Ridgecrest earthquake sequence, *J. Geophys. Res.* **126**, e2020JB020551, doi: [10.1029/2020JB020551](https://doi.org/10.1029/2020JB020551).
- Milliner, C. W. D., J. F. Dolan, J. Hollingsworth, S. Leprince, and F. Ayoub (2016). Comparison of coseismic near-field and off-fault surface deformation patterns of the 1992  $M_w$  7.3 Landers and 1999  $M_w$  7.1 Hector Mine earthquakes: Implications for controls on the distribution of surface strain, *Geophys. Res. Lett.* **43**, 10,115–10,124.
- Milliner, C. W. D., J. F. Dolan, J. Hollingsworth, S. Leprince, F. Ayoub, and C. G. Sammis (2015). Quantifying near-field and off-fault deformation patterns of the 1992  $M_w$  7.3 Landers earthquake, *Geochem. Geophys. Geosys.* **16**, 1577–1598.
- Moss, R. E. S., and Z. E. Ross (2011). Probabilistic fault displacement hazard analysis for reverse faults, *Bull. Seismol. Soc. Am.* **101**, 1542–1553.
- Nurminen, F., P. Boncio, F. Visini, B. Pace, A. Valentini, S. Baize, and O. Scotti (2020). Probability of occurrence and displacement regression of distributed surface rupturing for reverse earthquakes, *Front. Earth Sci.* **8**, doi: [10.3389/feart.2020.581605](https://doi.org/10.3389/feart.2020.581605).
- Oglesby, D. (2008). Rupture termination and jump on parallel offset faults, *Bull. Seismol. Soc. Am.* **98**, 440–447.
- Oglesby, D. D. (2020). What can surface-slip distributions tell us about fault connectivity at depth? *Bull. Seismol. Soc. Am.* **110**, no. 3, 1025–1036, doi: [10.1785/0120190245](https://doi.org/10.1785/0120190245).
- Olsen, K. B., R. Madariaga, and R. J. Archuleta (1997). Three-dimensional dynamic simulation of the 1992 Landers earthquake, *Science* **278**, 834–838.
- Oskin, M., L. Perg, D. Blumentritt, S. Mukhopadhyay, and A. Iriondo (2007). Slip rate of the Calico fault: Implications for geologic versus geodetic rate discrepancy in the Eastern California shear zone, *J. Geophys. Res.* **112**, doi: [10.1029/2006JB004451](https://doi.org/10.1029/2006JB004451).
- Oskin, M. E., J. R. Arrowsmith, A. H. Corona, A. J. Elliott, J. M. Fletcher, E. J. Fielding, P. O. Gold, J. J. G. Garcia, K. W. Hudnut, J. Liu-Zeng, et al. (2012). Near-field deformation from the El Mayor-Cucapah earthquake revealed by differential LIDAR, *Science* **335**, 702–705.
- Perfettini, H., and J. P. Avouac (2007). Modeling afterslip and aftershocks following the 1992 Landers earthquake, *J. Geophys. Res.* **112**, doi: [10.1029/2006JB004399](https://doi.org/10.1029/2006JB004399).
- Perrin, C., I. Manighetti, J. P. Ampuero, F. Cappa, and Y. Gaudemer (2016). Location of largest earthquake slip and fast rupture controlled by along-strike change in fault structural maturity due to fault growth, *J. Geophys. Res.* **121**, 3666–3685.
- Petersen, M. D., T. E. Dawson, R. Chen, T. Q. Cao, C. J. Wills, D. P. Schwartz, and A. D. Frankel (2011). Fault displacement hazard for strike-slip faults, *Bull. Seismol. Soc. Am.* **101**, 805–825.
- Peyrat, S., K. Olsen, and R. Madariaga (2001). Dynamic modeling of the 1992 Landers earthquake, *J. Geophys. Res.* **106**, 26,467–26,482.
- Philibosian, B., and A. J. Melzner (2020). Segmentation and supercycles: A catalog of earthquake rupture patterns from the Sumatran Sunda Megathrust and other well-studied faults worldwide, *Q. Sci. Rev.* **241**, doi: [10.1016/j.quascirev.2020.106390](https://doi.org/10.1016/j.quascirev.2020.106390).

- Ponti, D. J., J. K. Blair, C. M. Rosa, K. Thomas, A. J. Pickering, S. Akciz, S. Angster, J.-P. Avouac, J. Bachhuber, S. Bacon, *et al.* (2020). Documentation of surface fault rupture and ground deformation features produced by the Ridgecrest M 6.4 and M 7.1 earthquake sequence of July 4 and 5, 2019, *Seismol. Res. Lett.* **91**, 2942–2959.
- Power, W. L., and T. E. Tullis (1991). Euclidean and fractal models for the description of rock surface-roughness, *J. Geophys. Res.* **96**, 415–424.
- Quigley, M., R. Van Dissen, N. Litchfield, P. Villamor, B. Duffy, D. Barrell, K. Furlong, T. Stahl, E. Bilderback, and D. Noble (2012). Surface rupture during the 2010  $M_w$  7.1 Darfield (Canterbury) earthquake: Implications for fault rupture dynamics and seismic-hazard analysis, *Geology* **40**, 55–58.
- Rockwell, T. K., S. Lindvall, T. Dawson, R. Langridge, W. Letts, and Y. Klinger (2002). Lateral offsets on surveyed cultural features resulting from the 1999 Izmit and Duzce earthquakes, Turkey, *Bull. Seismol. Soc. Am.* **92**, 79–94.
- Roten, D., K. B. Olsen, and S. M. Day (2017). Off-fault deformations and shallow slip deficit from dynamic rupture simulations with fault zone plasticity, *Geophys. Res. Lett.* **44**, 7733–7742.
- Sagy, A., and E. E. Brodsky (2009). Geometric and rheological asperities in an exposed fault zone, *J. Geophys. Res.* **114**, doi: [10.1029/2008JB005701](https://doi.org/10.1029/2008JB005701).
- Sarmiento, A., N. Abrahamson, S. Baize, Y. Bozorgnia, R. Chen, K. J. Coppersmith, T. Dawson, J. Donahue, V. Jacob, M. Ketabdar, *et al.* (2019). A new model database for next-generation fault displacement hazard analysis, *Seismological Society of America Annual Meeting*, edited, Seattle, Washington.
- Savran, W. H., and K. B. Olsen (2020). Kinematic rupture generator based on 3-D spontaneous rupture simulations along geometrically rough faults, *J. Geophys. Res.* **125**, e2020JB019464, doi: [10.1029/2020JB019464](https://doi.org/10.1029/2020JB019464).
- Scharer, K., R. Weldon, G. Biasi, A. Streig, and T. Fumal (2017). Ground-rupturing earthquakes on the northern Big Bend of the San Andreas fault, California, 800 AD to present, *J. Geophys. Res.* **122**, 2193–2218.
- Shaw, B. E. (2011). Surface-slip gradients of large earthquakes, *Bull. Seismol. Soc. Am.* **101**, 792–804.
- Shi, Z., and S. M. Day (2013). Rupture dynamics and ground motion from 3-D rough-fault simulations, *J. Geophys. Res.* **118**, 1122–1141.
- Sieh, K., L. Jones, E. Hauksson, K. Hudnut, D. Eberhart-Phillips, T. Heaton, S. Hough, K. Hutton, H. Kanamori, A. Lilje, *et al.* (1993). Near-field investigations of the Landers earthquake sequence, April to July 1992, *Science* **260**, 171–176.
- Stepp, J. C., I. Wong, J. Whitney, R. Quittmeyer, N. Abrahamson, G. Toro, R. Youngs, K. Coppersmith, J. Savy, T. Sullivan, *et al.* (2001). Probabilistic seismic hazard analyses for ground motions and fault displacement at Yucca Mountain, Nevada, *Earthq. Spectra* **17**, 113–151.
- Tago, J., V. M. Cruz-Atienza, J. Virieux, V. Etienne, and F. J. Sanchez-Sesma (2012). A 3D hp-adaptive discontinuous Galerkin method for modeling earthquake dynamics, *J. Geophys. Res.* **117**, doi: [10.1029/2012JB009313](https://doi.org/10.1029/2012JB009313).
- Teran, O. J., J. M. Fletcher, M. E. Osokin, T. K. Rockwell, K. W. Hudnut, R. M. Spelz, S. O. Akciz, A. P. Hernandez-Flores, and A. E. Morelan (2015). Geologic and structural controls on rupture zone fabric: A field-based study of the 2010  $M_w$  7.2 El Mayor-Cucapah earthquake surface rupture, *Geosphere* **11**, 899–920.
- Thomas, M. Y., and H. S. Bhat (2018). Dynamic evolution of off-fault medium during an earthquake: A micromechanics based model, *Geophys. J. Int.* **214**, 1267–1280.
- Van Dissen, R., D. Barrell, N. Litchfield, P. Villamor, M. Quigley, A. King, K. Furlong, J. Begg, D. Townsend, H. Mackenzie, *et al.* (2011). Surface rupture displacement on the Greendale fault during the  $M_w$  7.1 Darfield (Canterbury) earthquake, New Zealand, and its impact on man-made structures, Paper presented at the *Ninth Pacific Conf. on Earthquake Engineering Building an Earthquake-Resilient Society*, Auckland, New Zealand.
- Vyas, J. C., P. M. Mai, M. Galis, E. M. Dunham, and W. Imperatori (2018). Mach wave properties in the presence of source and medium heterogeneity, *Geophys. J. Int.* **214**, 2035–2052.
- Wald, D. J., and T. H. Heaton (1994). Spatial and temporal distribution of slip for the 1992 Landers, California, earthquake, *Bull. Seismol. Soc. Am.* **84**, 668–691.
- Wang, Y., and S. M. Day (2017). Seismic source spectral properties of crack-like and pulse-like modes of dynamic rupture, *J. Geophys. Res.* **122**, 6657–6684.
- Wang, Y., and S. M. Day (2020). Effects of off-fault inelasticity on near-fault directivity pulses, *J. Geophys. Res.* **125**, doi: [10.1029/2019JB019074](https://doi.org/10.1029/2019JB019074).
- Wang, Y., S. M. Day, and M. A. Denolle (2019). Geometric controls on pulse-like rupture in a dynamic model of the 2015 Gorkha earthquake, *J. Geophys. Res.* **124**, 1544–1568.
- Wells, D. L., and K. J. Coppersmith (1994). New empirical relationships among magnitude, rupture length, rupture width, rupture area, and surface displacement, *Bull. Seismol. Soc. Am.* **84**, 974–1002.
- Wesnousky, S. G. (2008). Displacement and geometrical characteristics of earthquake surface ruptures: Issues and implications for seismic-hazard analysis and the process of earthquake rupture, *Bull. Seismol. Soc. Am.* **98**, 1609–1632.
- Withers, K. B., K. B. Olsen, S. M. Day, and Z. Shi (2019). Ground motion and intraevent variability from 3D deterministic broadband (0–7.5 Hz) simulations along a nonplanar strike-slip fault, *Bull. Seismol. Soc. Am.* **109**, 229–250.
- Wollherr, S., A. A. Gabriel, and P. M. Mai (2019). Landers 1992 “reloaded”: Integrative dynamic earthquake rupture modeling, *J. Geophys. Res.* **124**, 6666–6702.
- Yamashita, T. (2000). Generation of microcracks by dynamic shear rupture and its effects on rupture growth and elastic wave radiation, *Geophys. J. Int.* **143**, 395–406.
- Yoon, S. W., S. J. Kim, and D. Park (2020). Estimation of seismically induced longitudinal strain in pipelines subjected to incident shear wave, *KSCE J. Civ. Eng.* **24**, 2322–2332.
- Youngs, R. R., W. J. Arabasz, R. E. Anderson, A. R. Ramelli, J. P. Ake, D. B. Slemmons, J. P. McCalpin, D. I. Doser, C. J. Fridrich, F. H. Swan, *et al.* (2003). A methodology for probabilistic fault displacement hazard analysis (PFDHA), *Earthq. Spectra* **19**, 191–219.
- Zinke, R., J. Hollingsworth, and J. F. Dolan (2014). Surface slip and off-fault deformation patterns in the 2013  $M_w$  7.7 Balochistan, Pakistan earthquake: Implications for controls on the distribution of near-surface coseismic slip, *Geochem. Geophys. Geosys.* **15**, 5034–5050.

Manuscript received 16 March 2021